Electronic Supplementary Material (ESI) for Lab on a Chip.

Gel-on-a-Chip: Continuous, Velocity-Dependent DNA Separation using Nanoscale Lateral Displacement

Benjamin H. Wunsch[1,*], Sung-cheol Kim[1,*], Stacey M. Gifford[1], Yann Astier[1,3], Chao Wang[1,4], Robert L. Bruce[1], Jyotica V. Patel[1], Elizabeth A. Duch[1], Simon Dawes[1], Gustavo Stolovitzky[1,2], and Joshua T. Smith[1]

[1]IBM T.J. Watson Research Center, Yorktown Heights, NY
[2]Department of Genetics and Genomics Sciences, Icahn School of Medicine, Mount Sinai, New York, NY
[3]Current address: Roche Molecular Systems, Pleasanton, CA
[4]Current address: School of Electrical, Computer and Energy Engineering, Arizona State University, Tempe, AZ
[*]Corresponding author: bhwunsch@us.ibm.com, kimsung@us.ibm.com

March 13, 2019

Contents

1 Materials and Methods

Three separate type of chips were fabricated for this study, referred to here as Gen I, Gen II, and Gen III. Gen I chips (Fig. 1a, which measure 40 mm sq. and utilize frontside sample loading, contain six separate arrays for conducting independent experiments on a single chip and were used as the workhorse to broadly characterize displacement efficiency of dsDNA. Gen II (Fig. 4a) and Gen III (Fig. 5a) chips each measure 20 mm sq. and employ sets of microfluidic through-silicon vias (TSVs), or access holes, that permit sample loading from the backside of the chip, enabling faster time to experiment and smaller chip design. The Gen II design consists of a tri-loader configuration at the sample inlet to allow the introduction of jacketing buffers that confine sample introduction to the left-hand side of the array inlet, thereby enabling full separation of disparate dsDNA fragment sizes. The Gen III chip layout includes four large arrays (each $750\mu m$ wide) in parallel with shared outlets for sample collection and downstream analysis. The fabrication process for Gen I chips is described elsewhere [14].

Pillar arrays and other microfluidic features for the smaller Gen II and Gen III chips were defined using different lithography processes. In both cases, features were defined in a resist stack followed by successive pattern transfer first into a silicon dioxide (SiO2) hardmask (HM) and secondly into silicon using reactive-ion etching (RIE). For Gen II, a 2-step lithography process was used to define fluidic features similar to Gen I, combining electron beam (e-beam) and deep-ultra violet (DUV) lithography to create the nanoDLD pillar array features and adjoining microchannels, respectively. E-beam lithography was performed on a high-resolution VectorBeam 6 (Leica VB6HR) system to define high-resolution pillar arrays in a resist stack consisting of an HM8006 organic planarization layer (OPL) (JSR) coated with a thin 2% hydrogen silsesquioxane (HSQ) (Dow Corning) negative tone e-beam resist. After developing the exposed features, the wafers were coated first with a 60nm-thick developable bottom anti-reflective coating (DBARC) followed by a 0.45 μm-thick positive UV110 photoresist and all DUV microchannel regions were printed directly on top of and adjacent to the e-beam resist features using a 0.65 NA DUV stepper (ASML). The use of e-beam lithography allowed design flexibility to print arrays tailored to achieve a specific dsDNA size separation as shown in Fig. 1e,f,g without mask creation. In contrast, Gen III chips were printed using a single 193nm lithography process to define all microchannel and array features simultaneously using a 0.75 NA 193nm wavelength stepper (ASML). The Gen II resist stack was composed of 0.4μm HM8006 OPL (JSR), 35nm Si ARC, and a 160nm positive AR1570-16-35SD resist.

RIE was used to etch both the pillar array and microchannel features into silicon simultaneously. Optimized RIE processing was carried out in an DPSII ICP etch chamber (Applied Materials, CA) for pattern transfer to fabricate 300-500 nm high Si pillars from the resist patterns, depending on the desired gap width. For Gen II, the negative-tone HSQ resist was used to etch through the OPL using an N2/O2/Ar/C2H4 chemistry at 400 W source power, 100 W bias power and 4 mTorr pressure at 65 ^{o}C. Next, the SiO2 HM was patterned using CF4/CHF3 chemistry at 500 W source power, 100 W bias power and 30 mTorr pressure at 65 ^{o}C. The OPL carbon resist was stripped after HM patterning using O2/N2 chemistry in an Axiom downstream asher (Applied Materials, CA) at 250 ^{o}C. Finally, the patterned SiO2 HM was used to transfer the array and microchannel features into Si using the DPS II ICP etch system (Applied Materials, CA) by first a CF4/C2H4 native oxide breakthrough step and then a Cl2/HBr/CF4/He/O2/C2H4 main etch at 650 W source power, 85W bias power and 4 mTorr pressure at 65 ^{o}C. The Gen III etch process used was identical with the addition of a Si ARC breakthrough step using CF4/CHF3 chemistry at 500 W source power, 100 W bias power and 30 mTorr pressure at 65 ^{o}C in same DPS II ICP etch system. The recipes were used with varied run times to fabricate 200-450 nm high Si pillars and microchannel features, depending on the desired gap width and aspect ratio. After microfluidic features were RIE etched, residual organics were removed from wafers by submerging them in a bath containing a 10:1 mixture of sulfuric/nitric acid at 150 ^{o}C, after which the HM was removed in 10:1 dilute hydrofluoric (DHF) acid bath.

With the HM removed, the Gen II and Gen III chips underwent further processing to define sets of TSVs that enabled fluidic access to/from the back and front side of the chips. This feature allowed us to introduce fluid from the back side onto the chip much closer to the array inlets since the size of the objective lens on the fluorescence microscope no longer needed to be considered in this configuration. Further, this approach overcame the need for structured glass cover slips, and improved chip scalability, allowing a chip count of 52 chips per 200mm wafer compared to only 12 for Gen I. An optical contact MA8 mask aligner (Karl Suss) was used to lithographically define 200μm diameter via locations in a 10μm-thick AZ4620 (AZ Electronic Materials) resist applied on top of a layer of hexamethyldisilazane (HMDS) adhesion promoter. Vias were then RIE etched $\sim$550μm deep into the 725μm-thick 200mm diameter wafers. The deep fluidic vias are transferred into Si by inductively coupled plasma etching (Alcatel 601E) using a Bosch process with alternating pulses of SF6 300 sccm and C4F8 150 sccm at a temperature of 20 ^{o}C with source and bias powers of 1800 W and 80 W, respectively. The posted etched resist was removed in an O2 asher (Plasmatherm) with a 600W plasma followed by an AZ300T Photoresist Stripper (AZ Electronic Materials) at 60 ^{o}C. The 175μm of remaining silicon at the bottom of the TSVs was removed using bonding and polishing steps to open the vias for fluidic access. SC1 (H2O2:NH4OH:DI - 1:1:5 at 65 ^{o}C) cleaned glass handler wafers were bonded to the front side of the microfluidic device wafers using a 0.25μm ablation material and HD3007 bonding film annealed at 350 ^{o}C in an N2 ambient. Next, a course grind removed 175μm of silicon from the backside of the wafer and a final 50μm polish using a Nalco slurry was applied to remove surface roughness and ensure that all vias were open. A laser was raster scanned over the surface of the glass handle wafer to ablate the adhesion layer, effectively debonding the handle and device wafers.

The debonded device wafer underwent a several cleans to remove unwanted resist and debris. An O2 asher (Plasmatherm) with a 600W plasma was first applied followed by a series of wet cleans, including a 10 min piranha clean (a 5:1 volume ratio of 98% H2SO4 and 30% H2O2) to remove resist residues, 60 second 100:1 DHF dip, and SC1 and RCA clean processes. Final chip preparation involved growing a thin thermal dry oxide layer, ranging in thickness from 10 - 50 nm, over the surface of the wafers.

To complete the fluidic devices, a glass ceiling was bonded to the chips to provide a fluid seal and allow in situ fluorescence imaging. The details of bonding the full-width injection chips have been reported previously [13], briefly: Chips are sequentially cleaned in boiling 1%v/v aqueous Micro90 for 20min, boiling deionized water (Milli-Q, Merck Millipore, Billerica, MA) for 20min, then cold water for 20min. Glass cover slips for the full-width injection devices were obtained (Schott Glass, Germany) and machined with inlet ports; cover slips for the resolution and extraction experiments were obtained from Schott Glass and had no structure machining. Chips, along with 170μm thick cover slips machined with inlet ports, were then immediately transfered to 1:1 v:v H_2SO_4:H_2O_2 piranha solution for 60min at 90°. Bonding was performed in open air so all following steps were executed quickly: chips/slips were removed from the piranha solution and rinsed sequentially, by gentle agitation, in 2x 300 mL deionized water. Chips/slips were dried with an N_2 jet, avoiding touching any surface to avoid contamination. Chips were pocketed into a custom built metal L-shaped jig to hold the chip in alignment when bonding to the glass slip. Chips were dried first, set on the jig, and the jig covered with a glass hood to prevent dust settling while the slip was cleaned. The slip was applied carefully over the chip and a pair of tweezers used to pocket it into the jig, aligning it over the chip. The cover slip was then tapped gently on the edge with a tweezer to initiate a tacking bond. In the case of an air pocket defect forming, Teflon tweezers were gently rubbed over the void to squeeze out the air. Tacked chip/slip bonds are strong enough to transfer to a quartz glass holder and anneal. Annealing was performed in a Lindberg Blue 3" tube furnace (Thermo Scientific, Waltham, MA), ramping 6hr to 600°, holding for 60hr, then ramping 6hr to room temperature. Annealed bonded chips could withstand pressurization to 290p.s.i (20bar) or greater, sufficient for all testing.

Running nanoDLD Devices

Chips were wet using ethanol, submerging only the inlets for 20min to allow fluid to wick up to the outlets. Chips were then submerged in ethanol for 10min, then submerged in deionized water for 20min. Chips were run in custom-built fluid jigs composed of a mounting base and a connector plate through which HPLC fittings (IDEX Health & Science) were used to interface 1/16" tubing for fluid injection/pressurization. The connector plate has a viewing window to allow at x100 oil-immersion objective (N-Achroplan x100/1.25 oil, Zeiss, Germany) to be used for fluorescence imaging. Fluids could be introduced to a reservoir in the flow cell which covers the input ports of the chip. To reduce drying out of fluid from the devices, chips were immediately removed from deionized water and loaded/sealed into the flow cells. A Qmix syringe pump (Cetoni, Germany) was connected to the tubing with a 10mL syringe. Chips were injected with pure buffer (1xTE, 3% mercaptoethanol, 0.1% TWEEN 20) at 145p.s.i. (10bar), 10min, prior to sample loading and injection. Typically $10\mu L$ of sample was loaded into the fluidic reservoir for injection into chips. Imaging was carried out on a Scope.A1 upright fluorescence microscope (Zeiss) with an Andor iXon Ultra 897 EMCCD camera (Andor Technology, Oxford Instruments, UK). Imaging and pump control were done manually through a computer interface. Fluorescence imaging was done with a 470nm light-emitting diode and filter set (38HE, 470/40 excitation, 495 beam splitter, 525/50 emission, Zeiss). Videos were taken at 17.9 to 100ms, depending on contrast, with typically 200frames.

For full-width injection devices a single fluid line from the pump was necessary to run. For resolution separation experiments, the hydrodynamic focusing junction required three inputs - a sample input and two jacketing fluid inputs with pure buffer. The jacketing inputs were controlled with a single pump using a tee-junction in the tubing to distribute to the flow cell. The width of the injected beam was controlled manually by stepping the sample and jacket applied pressures. To control velocity, the applied pressure was measured and mapped to the *in situ* observed particle motion through particle tracking. Particle position was measured for a series of frames (typically 5-20) and the average flow velocity, v, calculated based on the time elapse per frame. Individual particles suitable for tracking were generally only obtainable at low pressures. The velocity as a function of applied pressure of the nanoDLD device, $c = v/\Delta P$ was calculated for each G, dsDNA N using four to five low pressure readings at 0.5-29p.s.i. (2bar), and extrapolated to high pressures assuming a linear response (SI Appendix, Fig. 18). In the case of small fragments ($< 0.25kb$) particle tracking could not be done and so average c for tested G was used. Operating pressure range for velocity control and resolution separation experiments was 7 - 217p.s.i. (0.5 - 15bar).

Running Lambda DNA Fragment Extraction Devices

Extraction fluidic chips were prepared as described above. Chips were purged with 1xTE buffer to 10min at 145p.s.i. (10bar) prior to sample injection. A custom built flow cell was used for interfacing the chip to the fluid pump. The flow cell, and all HPLC fittings, were cleaned in 10%v/v H_2O_2 aqueous solution for 30min, rinsed with deionized water, and then 1xTE buffer prior to loading the chip. The chip has two input ports; each was filled with 20uL sample DNA solution and injected simultaneously using a tee-junction in the tubing from the syringe pump. Samples were run at room temperature, in the dark, for 36hr at 145p.s.i. ($\sim 200 \mu m$ s^{-1}).

2 DLD Geometry

A deterministic lateral displacement (DLD) array consists of rows of pillars or posts, of diameter D_0, and center-to-center pitch λ. In the current work, the λ in the axial (length of array channel, x) and lateral (width of array channel, y) are equal. The difference λ - D_0 defines the gap size, G. Going axially between pillar rows, each row shifts laterally by a row shift distance, δ, such that after N axial rows, the pillar positions laterally have reset to the starting values. This defines a superlattice of $N\lambda \times \lambda$. The row shift fraction is defined as $\varepsilon = 1/N$. This glide translation generates a sideways shift in the pillars with an angle $\theta_{max} = \arctan(\varepsilon)$, termed the *geometric angle*. θ_{max} defines the maximum angle of displacement within the array.

The DLD separates particles based on their apparent size. In the first analysis of DLD, N defines the number of "fluid lanes" into which the flux in the gap G is split. The lanes can be numbered starting from one side of the gap to the next, following the direction of the pillar shift. The width β_1 of the first lane defines the critical diameter, $D_c = 2\beta_1$, which defines the transition between separated and unaffected species. For hard-shelled colloids such as polystyrene beads with diameter D_p, for $D_p < D_c$, the particle can remain within the first lane and follow its trajectory through the array. This trajectory threads the particles through the array, resetting every N rows back to the same lateral position. There is no net gain in lateral displacement as the particle traverses the array axially, and this process is termed *zigzag mode*. For $D_p \geq D_c$, the particle cannot remain within the first lane, its width splitting it between the first and subsequent lanes. When this particle reaches a pillar, it cannot follow the first lane's trajectory around the pillar, and is instead physically pushed laterally into the next flow lane. This process continues at each row, leading to a net lateral displacement, a process termed *bump mode*. The binary nature of bump and zigzag mode is only approximate; experimental results have shown a continum transition with angles of displacement (migration angle) $\theta < \theta_{max}$, termed *partial bump mode*. Diffusion, geometry and chaotic periodicity have all been demonstrated to generate partial bump mode scenarios.

Although it would be expected $D_c = G\varepsilon$, a more general formula $D_c = aG\varepsilon^b$ accounts for nonlinearities in the fluid flow lateral profile. Assuming parabolic flow within G, $a = 2\sqrt{1/3}$ and $b = 1/2$, although experimental and theoretical calculations suggest these values can be altered [7]. Recent analysis of the detail flow in an array unit cell [9] has shown the periodicity of a particle traversing array can be chaotic, leading to a modified D_c due to the aggregated effect of individual bump and zigzag events. As the flow pattern within the array bears on D_c, altering the pillar geometry from a cylindrical prism to triangular prisms or more complex cross-sections can alter the D_c [**McGrath:2014bl**].

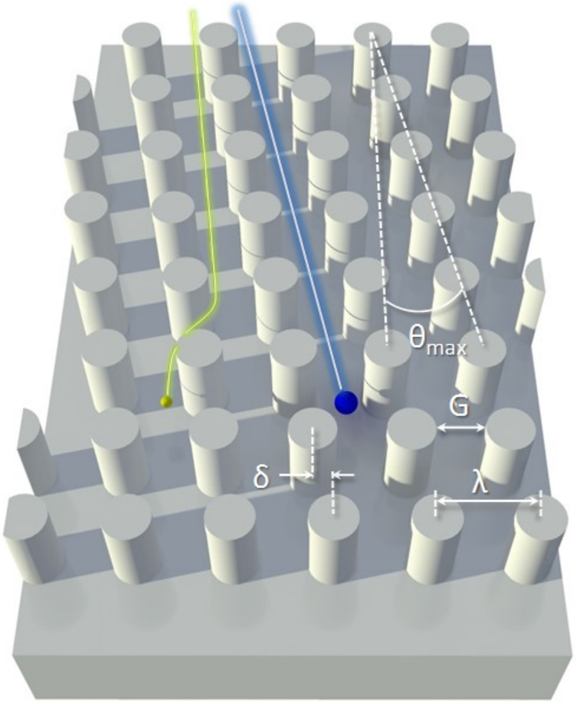

Figure 1: Schematic of nanoDLD array with pillar pitch λ, gap size between pillars G, row shift δ and geometric angle θ_{max}. The schematic shows a pillar array with periodicity $N = 6$, which gives a row-shift-fraction $\varepsilon = \delta/\lambda = 1/6$. The trajectory of particles with diameter $D_p < D_c$ winds every N' rows through the array (small sphere, yellow trace with $N' \geq N$), while for $D_p \geq D_c$, the particles are forced against pillars, causing an asymmetric lateral displacement of the particle along a trajectory with average migration angle $\theta = \theta_{max}$ (large sphere, blue trace). It is possible to also have particles with migration angles $0 \leq \theta \leq \theta_{max}$ due to diffusion, particle dispersity and asymmetric permeability in the fluid flow.

3 Fullwidth Injection Migration Angle Analysis and Displacement Efficiency

Full-width injection introduces samples into the nanoDLD across the entire width of the device. Lateral displacement of particles at a migration angle θ reduces the extent of the lateral particle flux in the lateral direction, with full bump mode $\theta = \theta_{max}$ causing all particle flux to concentrate against the side of the microchannel towards which θ_{max} slants, the collection wall. As lateral displacement is an algebraic progression, being the sum of independent bumping and/or zigzag events, the narrowing of the particle flux is linear along the axial direction of the array, and this produces a triangular wedge of particle density with an average angle of $\sim \theta$. θ can thus be obtained by analyzing the lateral displacement of the particle flux at the inlet and outlet of the nanoDLD array to determine the change in lateral width, ΔW, and using the formula $\theta = arctan(\Delta W/L)$ with L the axial length of the array. For all used full-width injection devices $L = 500\ \mu$m.

To obtain the lateral distribution of particle flux, we use fluorescence intensity as a reporter of dsDNA. This provides a readily readable signal of dsDNA distribution in the nanoDLD array, although the spread in the point source distribution of fluorescence means the DNA distribution does not correlate directly to the fluorescence; this leads however to a conservative estimate of displacement due to the light dispersion. Fluorescence micrograph videos of the inlet and outlet of the nanoDLD array are captured (200 frames, 0.0 18ms - 0.1 ms exposure times) and the videos compressed into average pixel intensity data arrays using ImageJ (U.S. National Institute of Health). Line profiles of the intensity are taken across the inlet and outlet interfaces and the profiles smoothed (50pt, fifth order polynomial Savitzky-Golay Filter, OriginPro, OriginLab Corp., MA). The edge of the fluorescence intensity profile, which is equated to the average extent of lateral displacement of the DNA fragment population, is calculated from the inflection point of the intensity profile, which is taken from the profile derivative. For fully bumped DNA, all fluorescence is concentrated into a narrow "jet" at the collection wall. In these cases the inflection point is hard to estimate due to the extended light spreading and is generally underestimated.

As the DLD modes are not binary, but can instead include a spectrum of migration angles (partial bump modes) between zigzag and bumping, it is useful to define a fractional geometric angle, $P = \frac{\theta}{\theta_{max}}$. Additionally, the displacement efficiency, η, is defined as:

$$\eta = \frac{\Delta W}{W} = \frac{tan\theta}{tan\theta_{max}} \approx \frac{\theta}{\theta_{max}} = P \tag{1}$$

The third equality stems from the fact that the migration angles are small ($< 10^\circ$) so the displacement efficiency is approximately equal to the fraction of geometric angle. η concisely denotes the displacement modes: $\eta = 0$ is zigzag mode, $\eta = 1$ is bump mode, and $0 < \eta < 1$ defines vales on the partial bumping spectrum. Particles of higher η displace to a greater degree than those with a low efficiency, and a curve of the displacement efficiency as a function of paricle size, D_p for a given array gap G, gives the characterization of the separation capability of a nanoDLD array (see SI Appendix, Fig. 5).

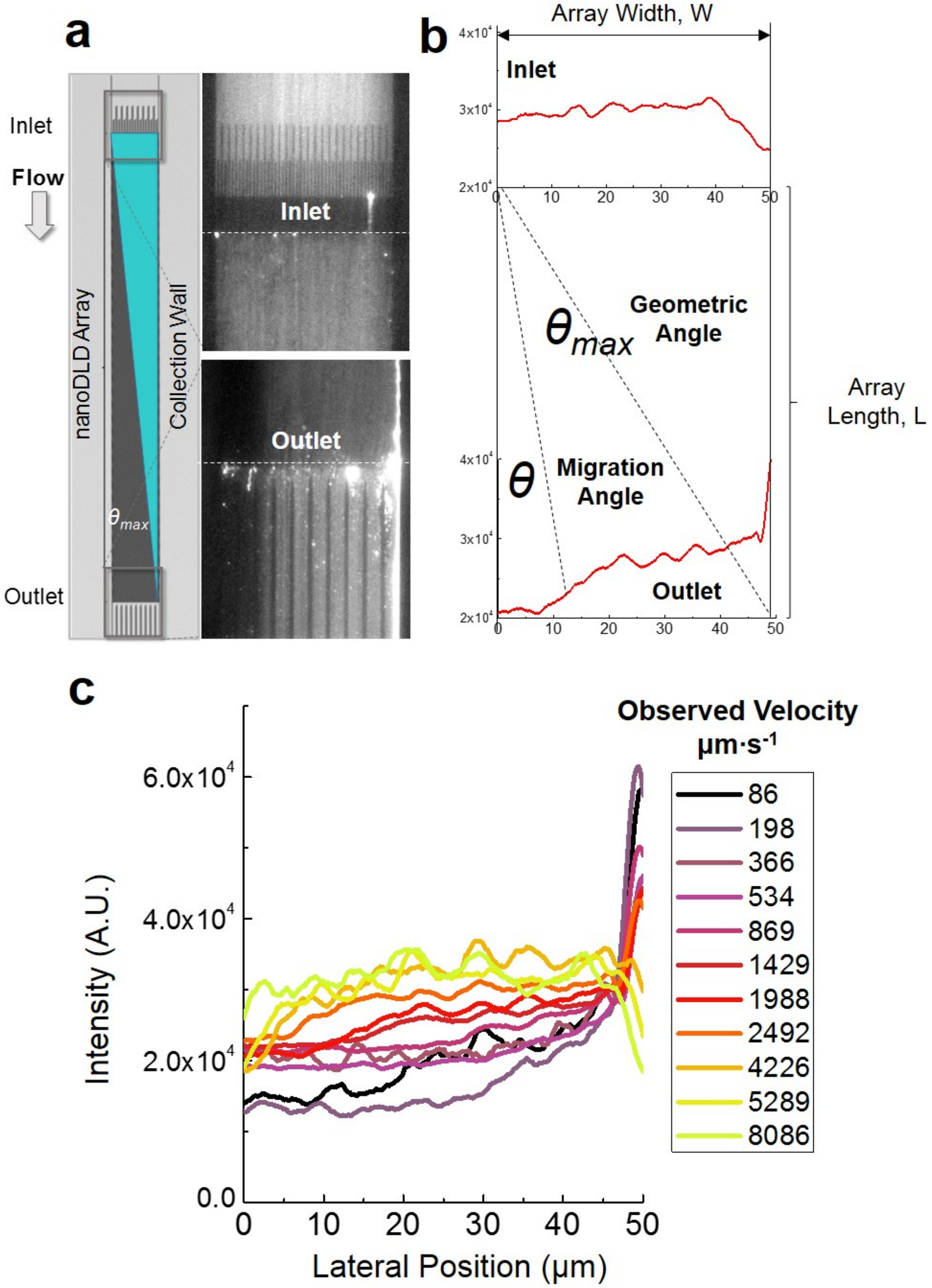

Figure 2: Full-width injection dsDNA in nanoDLD analysis. **(a)** Micrograph diagram of full width injection. DNA enters the array across the entire inlet and displaces along the slant of the geometric angle θ_{max} towards the collection wall (on the right). The distribution of DNA following a full-bump mode with $\theta = \theta_{max}$ is depicted by the triangular wedge. **(b)** Diagram plotting the inlet and outlet fluorescence intensity profiles of 2kb dsDNA in G = 250 nm array, showing how the DNA, which begins distributed across the width of the inlet, becomes concentrated into a narrower cross-section at the outlet, exemplifying lateral displacement. The sigmoidal rise at $\sim$ 10-20 μm is the transition from DNA depleted to enriched fluid, and its inflection point is used to define the migration angle θ. The flow velocity is 1,988 μm s^{-1}, at which 2 kb dsDNA partially bumps at a $\theta < \theta_{max}$. **(c)** Fluorescence intensity outlet profiles of 2 kb dsDNA in G = 250 nm as a function of flow velocity, showing the progression from partial bump to zigzag mode.

4 Comparison Spherical Bead and dsDNA Velocity Dependent Displacement Behavior

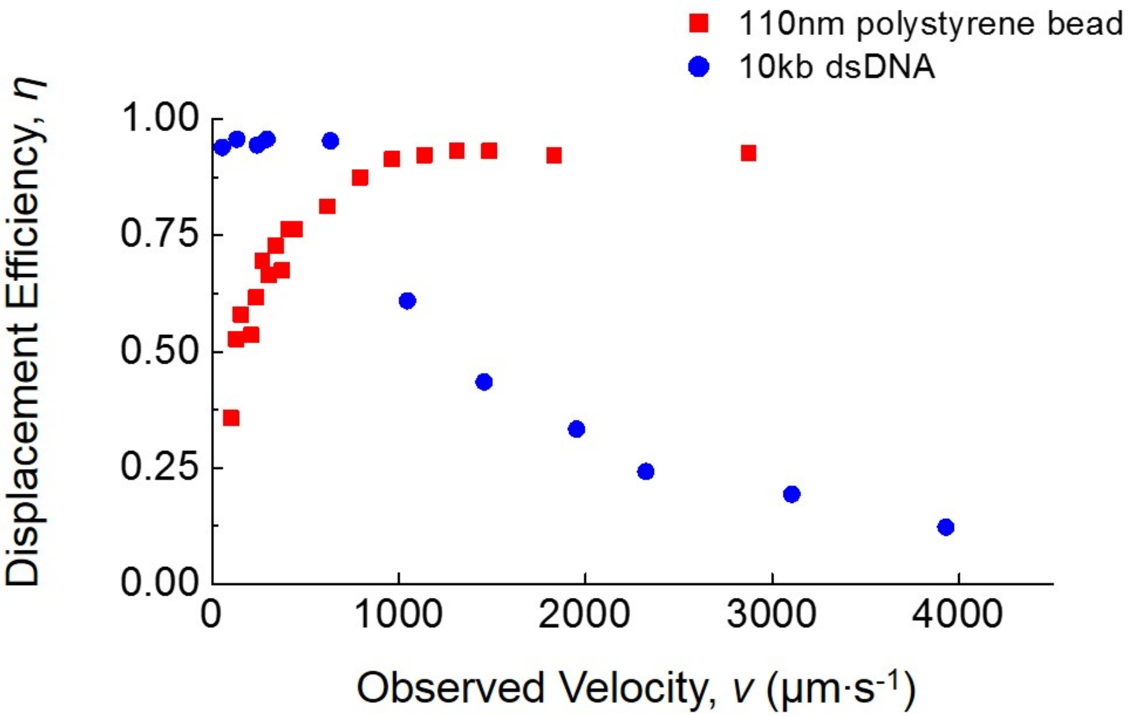

Figure 3: Displacement efficiency, η, as a function of flow velocity, v of a spherical 110nm polystyrene bead and 10kb dsDNA, showing the anti-correlation in their behaviors. Full width injection in a $G = 250$nm nanoDLD array for both species. The beads were run in 2%v/v TWEEN 20 solution in deionized water; the dsDNA was run in 1xTE buffer with 3%v/v β-mercaptoethanol and 0.1%v/v TWEEN 20.

5 Velocity Dependence of Displacement Efficiency of dsDNA

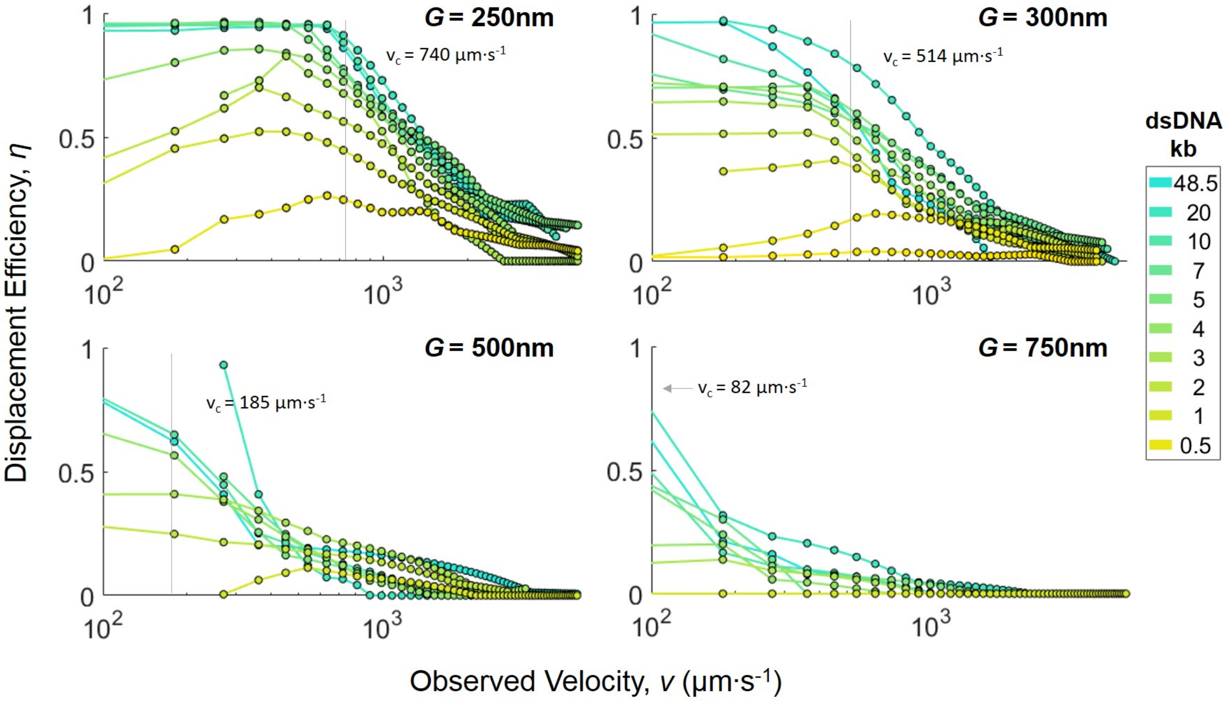

Figure 4: Displacement efficiency η as a function of observed flow velocity, v, for dsDNA of basepairs n in nanoDLD arrays of gap size G. The migration angle drop-off onset velocity values, v_c, are calculated from the de Genne's condition for polymer elongation (see SI Appendix on modeling). Curve points show interpolation of experimental data.

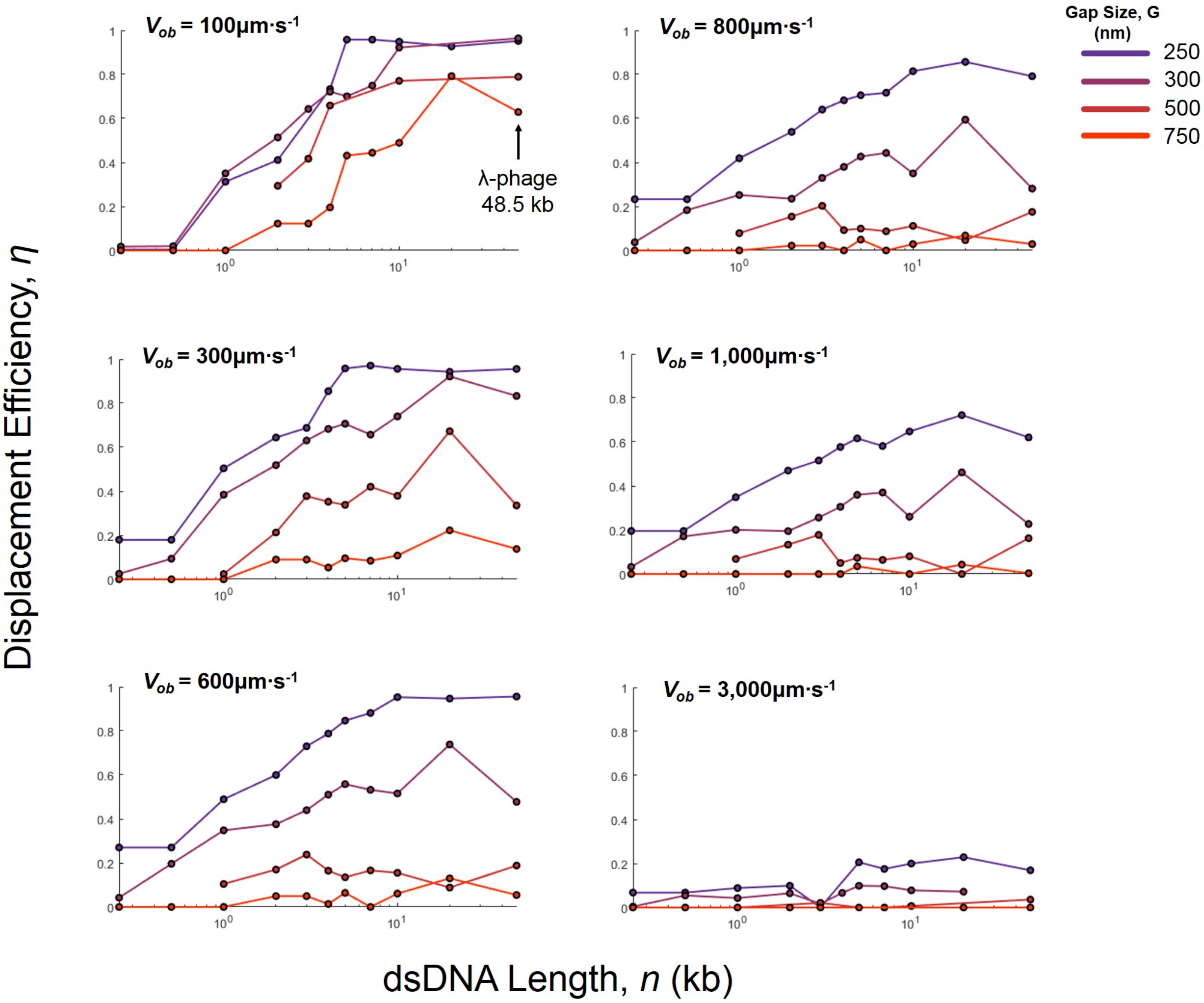

Figure 5: Displacement efficiency η as a function of dsDNa basepairs N for selected observed flow velocities v for the four gap sizes G tested.

6 Periodic Behavior and Capture Events

It was observed in the full width injection experiments, for longer dsDNA fragments (i.e. $n > 10$ kb), upon passing v_c that individual DNA particle trajectories would acquire a periodic pattern of bright and dim regions, as shown in 6. This periodicity is not observed below v_c and is not a consequence of aliasing from the camera; changing the exposure time does not change the lateral spacing of the period. Measurement of the average distance between high intensity regions in a trajectory, a, shows a rough correlation to the expected lattice constant of the array, $\langle a \rangle \sim N \lambda$. In zigzag mode, the particle trajectory side-winds to the adjacent pillar lane, resetting the particle position with respect to the periodicity. This zigzag transition occurs every $N\lambda$ along the array axis, i.e. every lattice repeat of the pillar array. The zigzag transition is expected to cause some slow down in the particle motion, as the particle transits through a stagnation point, thus it is reasonable to expect an increase in intensity, for a given exposure time, during this event. The correlation in periodicity with the pillar array lattice gives evidence that the dsDNA is in zigzag mode at these higher velocities.

Concomitant with the onset of periodicity in the DNA fragment traces, with increasing flow velocity the appearance and frequency of DNA capture events occurs. As seen in figure 7, dsDNA fragments become immobilized in the array in what qualitatively looks like a hairpin configuration. It is suggested these capture events represent individual (or clusters) elongated dsDNA molecules that became stuck on a pillar while threading through the array. Given the length of the event, it cannot represent a coiled dsDNA particle.

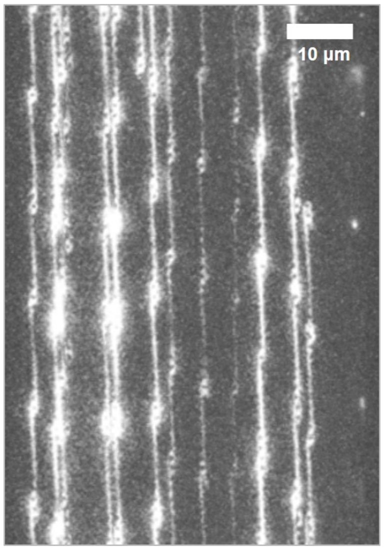

Figure 6: Fluorescence micrograph of the lambda phage genome, N = 48.5kb, in a G = 750nm array at $v \sim 2000 \mu m\, s^{-1}$, showing periodic intensity fluctuations axially along the array. The image is compressed from 200 frames, recording the maximum intensity of each pixel.

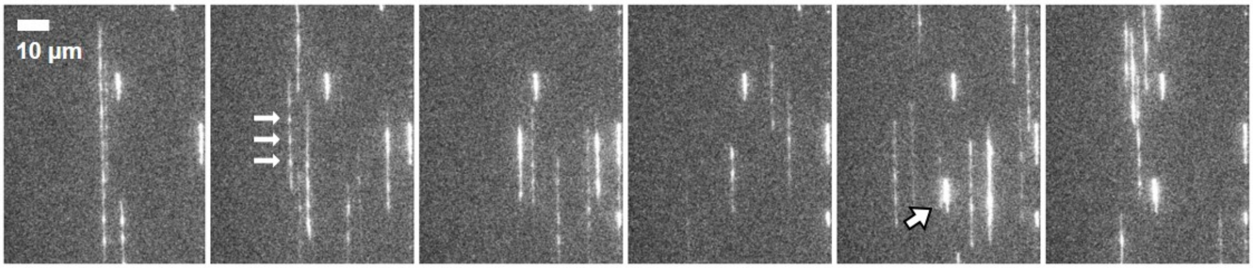

Figure 7: Fluorescence micrograph montage of lambda phage genome, N = 48.5kb, flowing in G = 250nm nanoDLD array at $v \sim 2000 \mu m\ s^{-1}$. The periodic intensity pattern can be seen in individual dsDNA particle trajectories (second frame, white arrows) as well as a capture event (fifth frame, white arrow) in which a dsDNA molecule has become immobilized in the array, appearing to straddle a pillar(s). Each frame is 18ms exposure; frames are drawn from a single 200 frame video but are not consecutive.

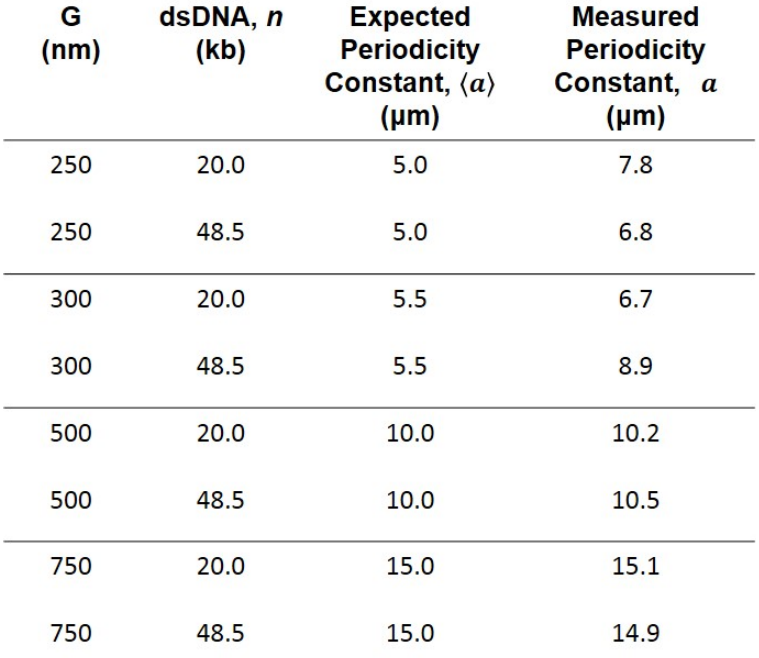

G (nm)	dsDNA, n (kb)	Expected Periodicity Constant, $\langle a \rangle$ (µm)	Measured Periodicity Constant, a (µm)
250	20.0	5.0	7.8
250	48.5	5.0	6.8
300	20.0	5.5	6.7
300	48.5	5.5	8.9
500	20.0	10.0	10.2
500	48.5	10.0	10.5
750	20.0	15.0	15.1
750	48.5	15.0	14.9

Table 1: Periodicity of dsDNA trajectories. The average spacing between high intensity spots along dsDNA molecule trajectory a (measured) and the expected spacing for the pillar array lattice $\langle a \rangle = N\lambda$ (expected). Data was collected for dsDNA for which the periodicity could be easily measured: 48.5kb (lambda DNA) and 20.0kb.

7 Critical Diameter Comparison for dsDNA in nanoDLD

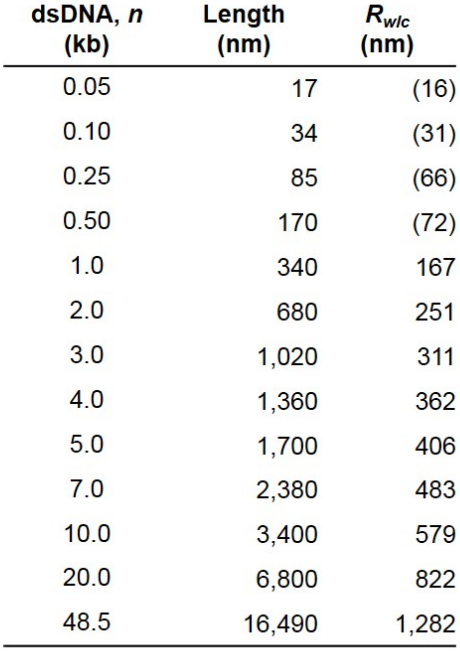

dsDNA, *n* (kb)	Length (nm)	R_{wlc} (nm)
0.05	17	(16)
0.10	34	(31)
0.25	85	(66)
0.50	170	(72)
1.0	340	167
2.0	680	251
3.0	1,020	311
4.0	1,360	362
5.0	1,700	406
7.0	2,380	483
10.0	3,400	579
20.0	6,800	822
48.5	16,490	1,282

Table 2: Estimated fragment length and worm-like-chain radius of gyration R_{wlc} for YOYO-1 dyed dsDNA tested. Here we used $R_{wlc} = \sqrt{2hpn\left(1 + \frac{p}{hn}\left(e^{\frac{-hn}{p}} - 1\right)\right)}$ where p = 50 nm is the persistent length, n is the number of base pairs, and h = 0.34 nm per basepair [12]. hn is the length of the dsDNA fragment in nanometers. Values in parentheses represent calculated radii which yield diameters larger than the length of the molecule, and are thus considered non-physical.

		Gap Size, G (nm)				
		78	**108**	**134**	**250**	**300**
$\eta = 0.95$	**n (kb)**	0.6	1.0	1.0	11.5	31.1
	R_{wlc} (nm)	103	174	165	621	1025
	$2R_{wlc}\,G^{-1}$	2.6	3.2	2.5	5.0	6.8
$\eta = 0.50$	**n (kb)**	0.3	0.5	0.6	3.2	5.6
	R_{wlc} (nm)	58	84	96	321	432
	$2R_{wlc}\,G^{-1}$	1.5	1.6	1.4	2.6	2.9
	D_c IDAS (nm)	31	43	54	100	120
	D_c HB (nm)	*	*	*	226	262

Table 3: Comparison of dsDNA fragment particle size, as estimated by the worm-like-chain radius of gyration, R_{wlc}, taken at two displacement efficiency values, η (inflection, η = 0.5 and estimated saturation, η = 0.95) to predicted critical diameter, D_c, for onset of bump mode in nanoDLD. N represents the basepair value taken at the selected efficiency value, as determined from a parametric fit of the experimental data. It is clear that all dsDNA fragments have estimated coil sizes larger than the gap size G. The scaling ratio $2R_{wlc}/G$ shows no constant correlation with G, as would be expected from standard DLD theory for hard-bodied spherical colloids. IDAS is from Inglis *et al* from $D_c = 0.4G$ for ε = 0.1, HB is from Heller, Bruss, which includes diffusion, for v = 400 $\mu m\ s^{-1}$. * Estimates of these values are nonphysical as theory predicts D_c is larger than G.[**Heller:2008jra**, 3, 6]

8 Reverse Flow of dsDNA in a nanoDLD Array

To provide evidence that the nanoDLD lateral displacement mechanism was not fragmenting the dsDNA during separation, focused injected 10kb DNA was run in a $G = 219$nm at $v = \sim 600\mu m\ s^{-1}$. The DNA jet fully bumps in this operation, exiting the array at the outlet. When the fluid flow is reversed, the 10kb dsDNA is forced backwards through the array. It is observed, SI Appendix, Fig. 8, that the reprocessed dsDNA again fully bumps and displaces to the opposite channel wall. If the dsDNA had been fragmented, such that at least some fragments have $n < 10$kb it would be expected to see individual particle events in which $\theta < \theta_{max}$. As is, all particles exhibit the same θ_{max} giving qualitative evidence that the DNA is not being damaged during processing.

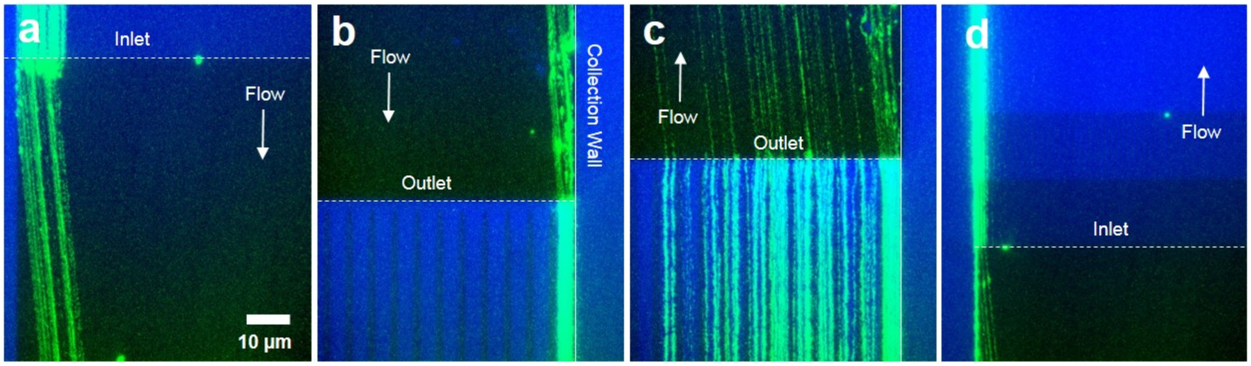

Figure 8: Fluorescence micrographs of 10kb dsDNA processed sequentially in the forward and then reverse direction in a $G = 219$nm nanoDLD array to demonstrate lateral displacement does not fragment the DNA. **(a)** 10kb dsDNA jet in forward flow at $v = \sim 600\mu m\ s^{-1}$, showing full bumping in **(b)**. **(c)** The same dsDNA reversed to flow backwards into the nanoDLD array through the outlet. The jet of dsDNA has broadened due to the diffusion of DNA particles during the time ($\sim$ 3min) required to switch the fluid pressurization. **(d)** Image at the inlet in reverse flow, at $v = \sim 600\mu m\ s^{-1}$, showing dsDNA is still fully bumping despite being processed through the nanoDLD array. No stray particle events were captured during imaging for 10min, suggesting a minimum amount of DNA fragmentation.

9 Displacement without TWEEN 20 Surfactant

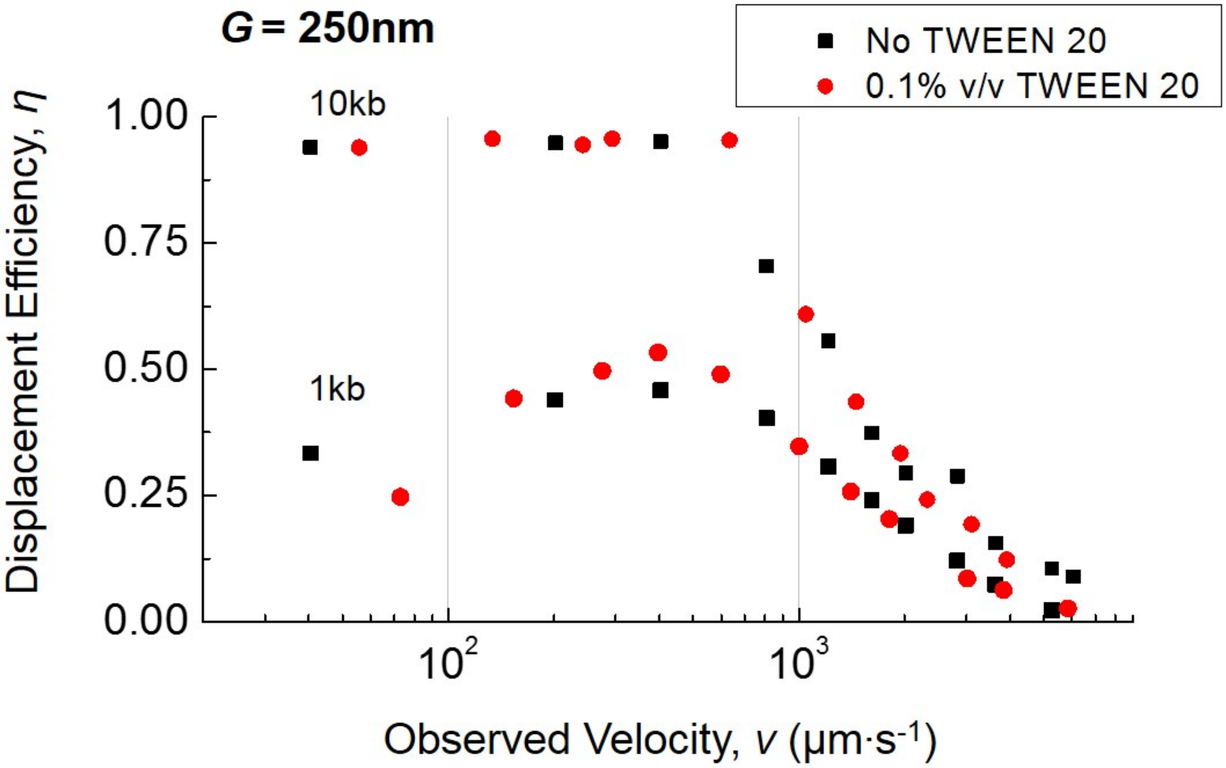

Figure 9: Plot of displacement efficiency as a function of flow velocity for 1kb and 10kb dsDNA fragments in a G = 250nm array in buffer with and without TWEEN 20 surfactant, showing no effect of the surfactant on the displacement and suggesting it is not causing compaction of the dsDNA. Buffer is 1xTE.

10 Modeling dsDNA Displacement in nanoDLD

10.1 Effective diameter of tethered ds-DNA changes in shear flow

When one end of a DNA molecule is held fixed to a surface while the other end is free, the DNA is considered *tethered*. Tethered DNA in a steady state fluid flow feels a drag force caused by the fluid, which pulls on the DNA and causes it to extend and elongate. A coil-stretch transition occurs when the entropy of the DNA coil is overcome by forces applied from the flowing fluid, pulling the polymer into a fully extended chain [**Perkins:1995ei**]. Thus the nature of the coil-stretch transition depends heavily on the fluid flow profile and velocity, which in turn determine the drag force on the polymer chain. It is difficult to calculate the drag force directly because the shape of DNA coil and the molecular interactions with the fluid change simultaneously. Assuming the coil has a spherical shape, the drag force can be calculated as follows:

$$f_D = 6\pi\eta_w va$$

where a is coil radius and v is the stead-state fluid velocity set at infinite, and η_w is the viscosity of water. In the case of a prolate ellipsoid, the drag force can be expressed as follows:

$$f_D = \frac{4\pi\eta_w va}{\log(a/b)} \quad \text{for} \quad a \gg b$$

with the major axis a and minor axis b of the ellipsoid. When the velocity is small, the elongation of the DNA molecule is minor and we can use a spherical estimation of the coil. However, when the velocity increases, the elongated DNA is assumed to take on an ellipsoid shape and we use the later formula.

Marko and Sigga suggested using the extension given by the end-to-end distance ($Ly = \vec{R}(L) - \vec{R}(0)$) as a parameter to interpolate the drag force in both the weak and strong forces. [11] Here, L is the contour length and $\vec{R}(s)$ is the positional vector parameterized by the distance s from one end. The interpolated drag force on a tethered DNA by the flow can be expressed as follows:

$$f_D = \frac{4\pi\eta_w v\alpha(Ly/2 + R_H)}{\log(1 + Ly/[2R_H]) + 2\alpha/3} \tag{2}$$

where $R_H = 0.375\sqrt{AL}(1-y^2)$, A is the persistence length of dsDNA, and α is an $O(1)$ fitting parameter. Here, $\alpha = 0.25$ is used, as determined in [11]. R_H is chosen so that it gives the correct value when $y \to 0$. The above formula gives $f_D = 6\pi\eta_w vR_H$ when the DNA coil becomes a sphere with radius $R_H = 0.375\sqrt{AL}$. Here, the prefactor of 0.375 is obtained from a microscopic calculation for the Zimm diffusion contant.[11]

The extension force for the worm-like-chain (WLC) model can be expressed in terms of the extension y as follows:

$$\frac{f_E A}{k_B T} = y + \frac{1}{4(1-y)^2} - \frac{1}{4} \tag{3}$$

where f_E is a extension force and A is a persistent length k_B and T are the Boltzmann constant and a temperature, respectively. For DNA in a typical solution, the persistent length A is $\sim 50\ nm$.[10] Unlike other common bio-polymers, double strand DNA has a long persistent length, which increases the threshold drag force needed to uncoil it.

By combining eq. 2 and 3 we can solve the extension y with a specific fluid velocity v. In a nanoDLD array, a DNA molecule can flow freely through the pillar array, and thus there is no force due to a fixing of one end of the molecule, as in the tethered scenario. There are two possible scenarios which may mimic tethering of the DNA and thus generate an elongating drag force in nanoDLD: (1) Near a pillar surface a stagnation point the fluid velocity can approximate an elongating force field, cause a large shear flow. (2) A DNA molecule can straddle a pillar, becoming captured or "hooked" around the pillar. In either scenario, the effect of pinning of the DNA temporarily can cause a extension force to develop, as describe for a tethered DNA particle. Following this reasoning, we modify the tethered drag force equation to approximate the drag inside a DLD array $f_{D,DLD}$ using the following equation:

$$f_{D,DLD} = \kappa_{DLD} \cdot f_D$$

where κ_{DLD} is a coefficient to adjust the drag force in a nanoDLD to match with a tethered DNA force. From experimental data, $\kappa_{DLD} = 0.5$ and this can be explained by the shear force in parabolic velocity profile between the pillars. In Marko's paper, the flow has constant velocity and shear force over the hydrodynamic radius of DNA is constant. However, in DLD array, the parabolic velocity profile gives a linear shear rate from 0 to γ_{max} and the shear stress over DNA gives roughly half of the force in a tethered DNA case.

In previous experiments done by Perkins, the end-to-end distance of the DNA coil was approximated from the contour length, z_{ob}, taken from fluorescence imaging of DNA molecules under optical microscopy [**Perkins:1995ei**]. Therefore, the observed length z_{obs} should be corrected to be the radius of gyration when the weak force $y \to 0$. The observed extension and the effective transverse diameter are following.

$$\begin{aligned} z_{obs} &= Ly + \sqrt{2AL}(1 - y^2) && (4) \\ R_H &= 0.375\sqrt{AL}(1 - y^2) && (5) \end{aligned}$$

Therefore, we can calculate the extension and the transverse diameter of DNA in a steady flow as shown in Fig. 10. The extension is the observed length, and the perpendicular diameter is $2R_H$. The graph shows the coil-stretch transition over different velocities and how the extension in the axial direction causes a decrease in the perpendicular diameter (cross-section) of the DNA coil. Here, for the calculation, we use the Brent's method in python scipy module for finding a root [8].

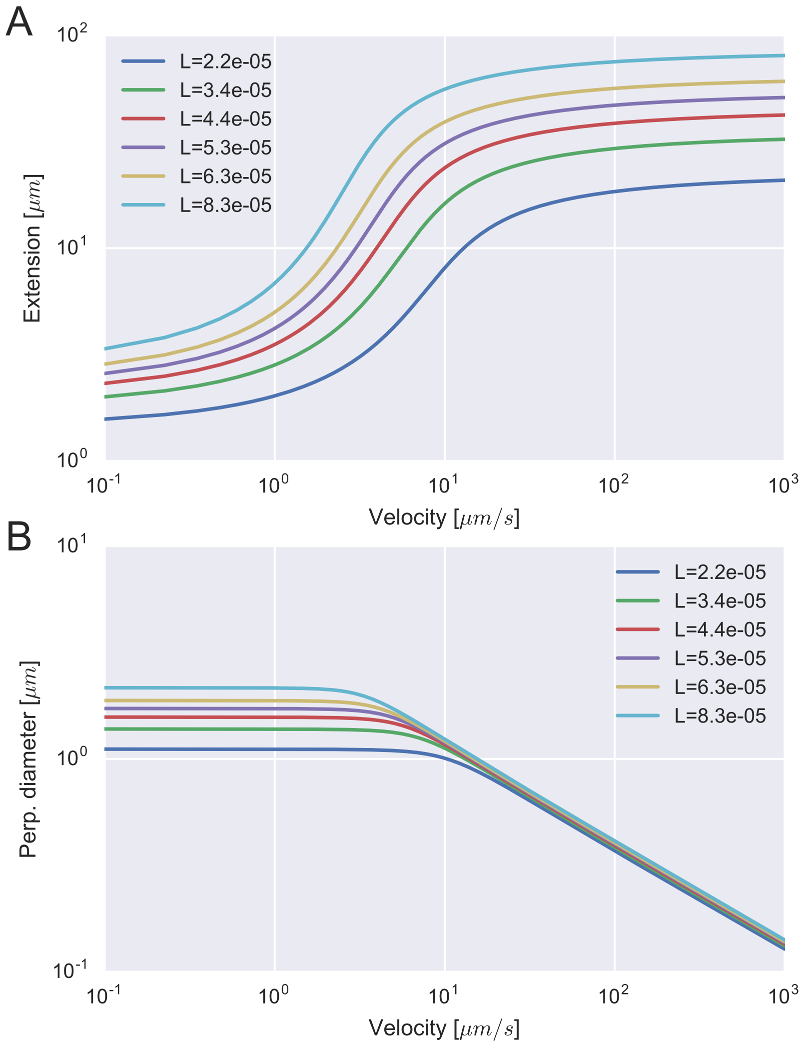

Figure 10: The extension length and the transverse radius of a tethered DNA by different fluid velocity. Here, we use a drag force coefficient $\alpha_D = 0.5$ and the confined diffusion coefficient $D^* = 0.2$.

10.2 Bumping probability varies on the effective diameter

Diffusion effects on a particle trajectory in DLD has been studied in several models. In Inglis's paper, the flow is assumed to have a parabolic profile and the total flux is divided into N streamlines. Due to the property of Laminar flow, streamlines do not mix with each other. [7] In Heller's paper, they used the model of Inglis and assumed a point-like pillar to calculate the distance of diffusion. [**Heller:2008jra**] They develop an escaping probability, which is opposite of the bumping probability, to take into account the effect of diffusion on θ. The escaping probability is calculated for a $1/N$ flux lane, where a particle with a finite diameter resides. Here, we follow their arguments and connect this escape probability into the migration angle.

In a point-like pillar array, the flow streamlines are straight lines, and by the symmetry of the pillar array the flow between two pillars is divided into N flux streams, each with identical flux, and each of width G/N. However; if we consider the parabolic velocity profile between pillars, to keep each stream of equal flux, the width should be calculated using the velocity distribution. Therefore, the lateral displacement of a particle with diameter (d) can be calculated as following.

$$l_{disp} = n_1 \frac{D_y}{N} = D_y \frac{d^2}{4G^2}(3 - \frac{d}{G}) \tag{6}$$

where D_y is the pitch distance in the direction perpendicular to flow and N is the structural periodicity (axial lattice constant) of the pillar array. n_1 is relative lane position due to the particle diameter:

$$n_1 = \frac{N}{Gu_0} \int_0^{d/2} u(y) dy = N \frac{d^2}{4G^2} \left(3 - \frac{d}{G} \right)$$

where G is the gap size between two adjacent pillars, and $u(y)$ is the velocity in the y-direction perpendicular to the flow:

$$u(y) = 6u_0 \frac{y}{G}(1 - \frac{y}{G}) \tag{7}$$

Therefore, l_{disp} is the displaced position in terms of an equal flux lane.

A particle located at l_{disp} will go between pillars in the axial direction and end at other side of the gap. We can define an unit cell, consisting of a lattice formed from the pillars in two adjacent rows, such at the edges of the unit cell are the axial and transverse gaps between pillars. Because each pillar has zero radius, the streamlines are not perturbed and the travel distance is D_x. If we assume a random walk along the travel trajectory, the lateral dispersion can be calculated:

$$\sigma^2(d, v) = 2\omega_{DLD} D\tau = 2\omega_{DLD} \left(\frac{k_B T_r}{3\pi\eta_w d} \right) \frac{D_x}{u_0}$$

where ω_{DLD} is a relative ratio between the bulk diffusion coefficient and one in a confined structure. τ is the flight time, which can be calculated by D_x/u_0. And η_w and k_B, T_r are the viscosity of water, Boltzmann constant, and room temperature, respectively. In the second step, we use the Stokes-Einstein relation to calculate the bulk diffusion constant. Here, accounting for the DNA's lateral confinement between the two pillars (surfaces), the diffusion constant is suppressed by a factor $\sim$ 2 to 5 resulting in ω_{DLD} = 0.2 to 0.5. [4] Note that the displacement depends on the particle diameter (d) and the mean velocity (u_0).

We can calculate the migration angle from the particle trajectory with the diffusion distance. In high velocity (high Péclet number), the migration angle θ should be in bumping mode or zig-zag mode:

$$\tan\theta \rightarrow \frac{D_y}{ND_x} (= \theta_{max}) \quad \text{or} \quad 0$$

where θ_{max} is the structural migration angle from pillar arrays. With diffusion, we can view the trajectory inside an unit cell with bumping and escaping probabilities as shown in Figure 11. The expectation value of

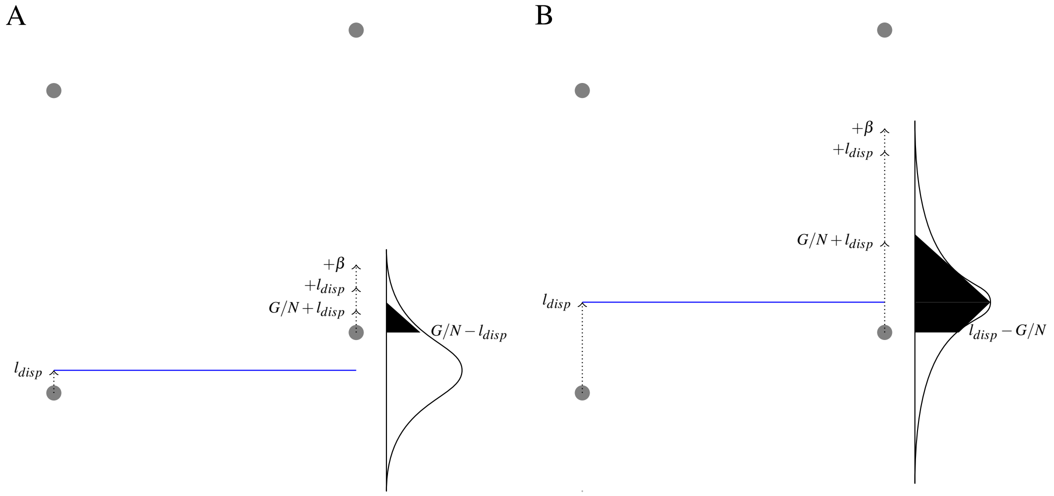

Figure 11: Unit cell trajectory and its probability (A) the simplified trajectory and its probability when particle diameter is smaller than the critical diameter (B) trajectory and probability when the particle diameter is larger than the critical diameter

the migration angle becomes the sum of two cases: (1) jump in bump mode and (2) jump in zig-zag mode:

$$\tan\langle\theta\rangle = \frac{D_y}{ND_x}\left(0 \cdot P_{down} + 1 \cdot P_{up}\right)$$

where P_{down} is the probability of a particle trajectory moving to make a zig-zag event (in the orientation depicted, the move being downwards), regardless if its size is bigger than the critical diameter or not. P_{up} is the probability of a particle trajectory ending in a position from G/N to $G/N + l_{disp} + \beta$ so that the migration angle becomes exactly θ_{max} (in the orientation depicted, the particle moving upwards). If the trajectory ends in a position higher than $G/N + l_{disp} + \beta$, it will give a migration angle higher than the structural angle (θ_{max}) but this probability is low and can be effectively ignored. In the two cases of particle diameter (1) larger than the critical diameter and (2) smaller than the critical diameter, ($l_{disp} < G/N$ or $l_{disp} > G/N$), the probability of upward movement is:

$$P_{up} = \frac{1}{2}\text{erf}\left(\frac{l_{disp} - G/N}{\sqrt{2}\sigma}\right) + \frac{1}{2}\text{erf}\left(\frac{l_{disp} + G/N + \beta}{\sqrt{2}\sigma}\right)$$

Where *erf* is the error function. The first term becomes negative when the diameter is less than the critical diameter and gives a smaller probability of moving upward. This first term becomes positive when the particle diameter is higher than the critical diameter so that the upward probability becomes significant. The second term sets the limit on how much the trajectory can displace upward so that the migration angle become θ_{max}. We can find the term β by considering the asymptotic behavior of the migration angle. Overall, the migration angle can be written as follows:

$$\tan\langle\theta\rangle = \frac{D_y}{ND_x}\left(\frac{1}{2}\text{erf}\left(\frac{l_{disp} - G/N}{\sqrt{2}\sigma}\right) + \frac{1}{2}\text{erf}\left(\frac{l_{disp} + G/N + \beta}{\sqrt{2}\sigma}\right)\right)$$

This simplified formula can be verified by looking at the asymptotic behavior when $u_0 \to \infty$. In this case, $\sigma \to 0$ and the erf function becomes +1 when $l_{disp} > G/N$ and -1 when $l_{disp} < G/N$. This yields a migration angle of θ_{max} or 0, respectively. When $u_0 \to 0$, $\sigma \to \infty$. By Taylor expansion of the error function, the migration angle becomes:

$$\tan\langle\theta\rangle \sim \frac{D_y}{ND_x}\left(\frac{l_{disp}}{\sqrt{2}\sigma} + \frac{\beta}{2\sqrt{2}\sigma}\right)$$

In the case of $l_{disp} > 0$, the migration angle become zero as long as β is not infinity. However, when $l_{disp} \to 0$ (the particle size is extremely small), the migration angle should be zero or linearly dependent on l_{disp} due to high diffusion. Therefore, β should be zero. This result is shown in Fig. 12. Here, the diameter of a particle is constant over the velocity.

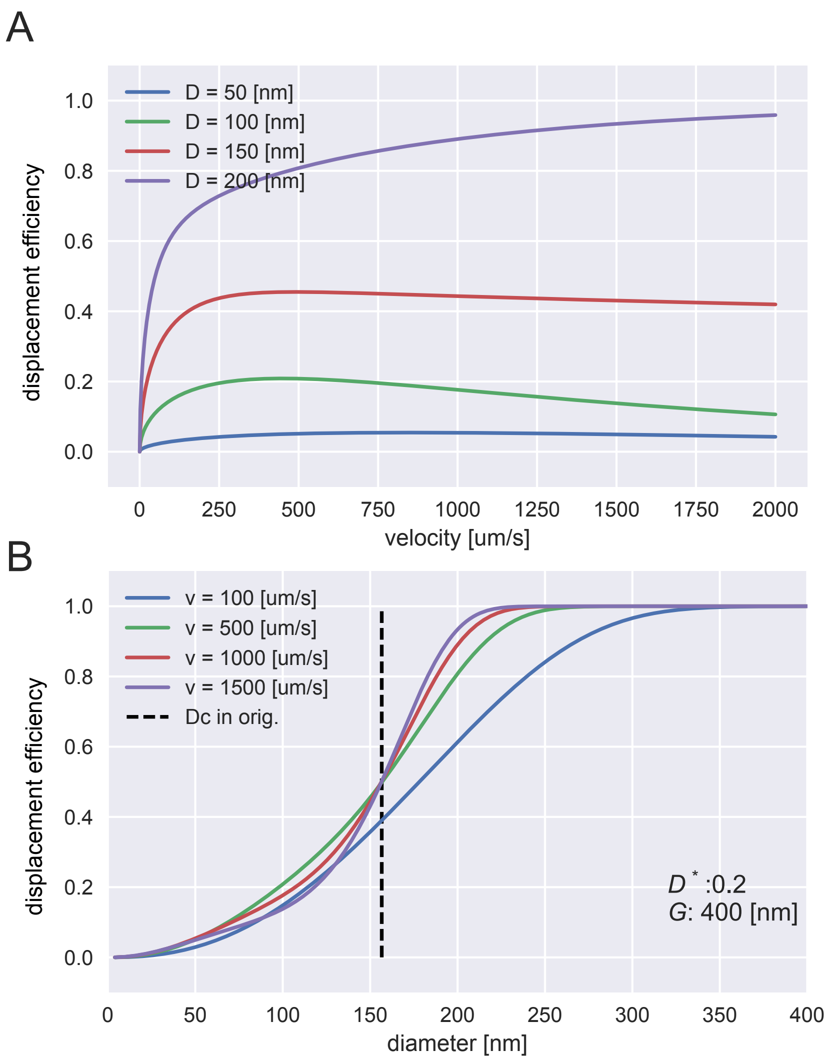

Figure 12: The relative migration angle of particles with different velocities and diameters. (A) The relative migration angle over velocities with different particle diameters. (B) The relative migration angle over particle diameters with different velocities.

10.3 DNA migration angle due to coil-stretch transition

In the case of DNA, we must consider the multiple, simultaneous effects of velocity on the molecule's behavior. As velocity increases, the drag force on a DNA increases due to the shear flow. This causes elongation of the DNA and concomitant decreasing of the perpendicular diameter (cross-section) of the DNA coil, assuming a conservation of coil volume. The change in the perpendicular radius causes two effect: (1) Modification of the effective coil diffusivity and (2) modification of the coil "size" with respect to the nanoDLD array's critical diameter.

To confirm the effect of the velocity on the migration angle in the case of DNA, we can check the velocity dependence of two terms as follows:

$$l_{disp} \sim R_H(v)$$

and

$$\sigma \sim 1/(R_H(v)v)$$

where R_H is the perpendicular radius of the elongated DNA. The migration angle can be written:

$$\tan\langle\theta\rangle = \frac{D_y}{ND_x}\left(\frac{1}{2}\text{erf}\left(\frac{l_{disp}(v) - D_y/N}{\sqrt{2}\sigma(v)}\right) + \frac{1}{2}\text{erf}\left(\frac{l_{disp}(v) + D_y/N}{\sqrt{2}\sigma(v)}\right)\right) \tag{8}$$

where $l_{disp}(v)$ and $\sigma(v)$ represent the velocity dependence. When $v \to 0$, $l_{disp} \to R_H \sim R_g$ where R_g is the radius of gyration of DNA and $\sigma \to \infty$. From this, the migration angle goes to zero. As velocity increases, the diffusion decreases and the migration angle increases. But when the radius of DNA decreases (due to the coil-stretch transition) once R_H reaches the critical diameter, the first term of equation 8 becomes negative and the migration angle decreases. When $v \to \infty$, $\sigma \to 0$ and $l_{disp} \to 0$. Therefore, the migration angle becomes zero again. This results are shown in Figure. 13

A key result from the previous arguments of velocity on diffusion and coil cross-section is the appearance of the drop-off velocity, v_c, at a characteristic value that is roughly independent of the DNA length. This onset of the migration angle drop-off due to the coil-stretch transition can be seen in a different way, using the arguments of Chen *et al* [**Chen2015**]. Using the de Gennes' criterion for the Weissenberg number ($Wi = \dot{\gamma}\tau$) in the case of elongation flow: [5]

$$\dot{\gamma}\tau \sim 1 \tag{9}$$

where $\dot{\gamma}$ is shear force on the DNA and τ is the relaxation time of DNA. In a DLD array, we can estimate the shear force from the parabolic velocity profile in equation 7.

$$\dot{\gamma} = \frac{du(y)}{dy} = \frac{6u_0}{G}\left(1 - \frac{2y}{G}\right)$$

where u_0 is the mean velocity of the flow. In experiments, the elongated DNA length is longer than a single pillar row (unit lattice), and thus the elongated DNA molecule must pass through multiple pillar rows, leading to the measured velocity averaging approximately to the maximum velocity ($u_{max} = 2/3u_0$). However, the maximum shear force happens near the pillar surface having a value of $\dot{\gamma}_{max} = 6u_0/G = 4u_{max}/G$.

For the relaxation time, we can use the scaling relation [5]:

$$\tau \sim \frac{0.2\eta_w R_{coil}^3}{k_B T}$$

where η_w is the dynamic viscosity of water ($\eta = 8.9 \times 10^{-4}\text{Pa}\cdots$) and R_{coil} is the radius of DNA in coil state. In DLD array, due to the average nanoconfinement of the pillars on the DNA coil, we can estimate the coil radius as $G/2$. Note this is a simplified version of the confinement effects on R_H given above. By combining equation 9 with those above, we can calculate the transition velocity v_c as follows:

$$v_c \sim 10\frac{k_B T}{\eta_w G^2}$$

This transition velocity is shown in Figure 13. Note that in the case of large gap size (e.g. $G = 750$nm), the transition velocity is small. Therefore, in the case of micro-scale DLD, for typical flow speeds, the dsDNA is in the stretched state and would show only a zigzag mode.

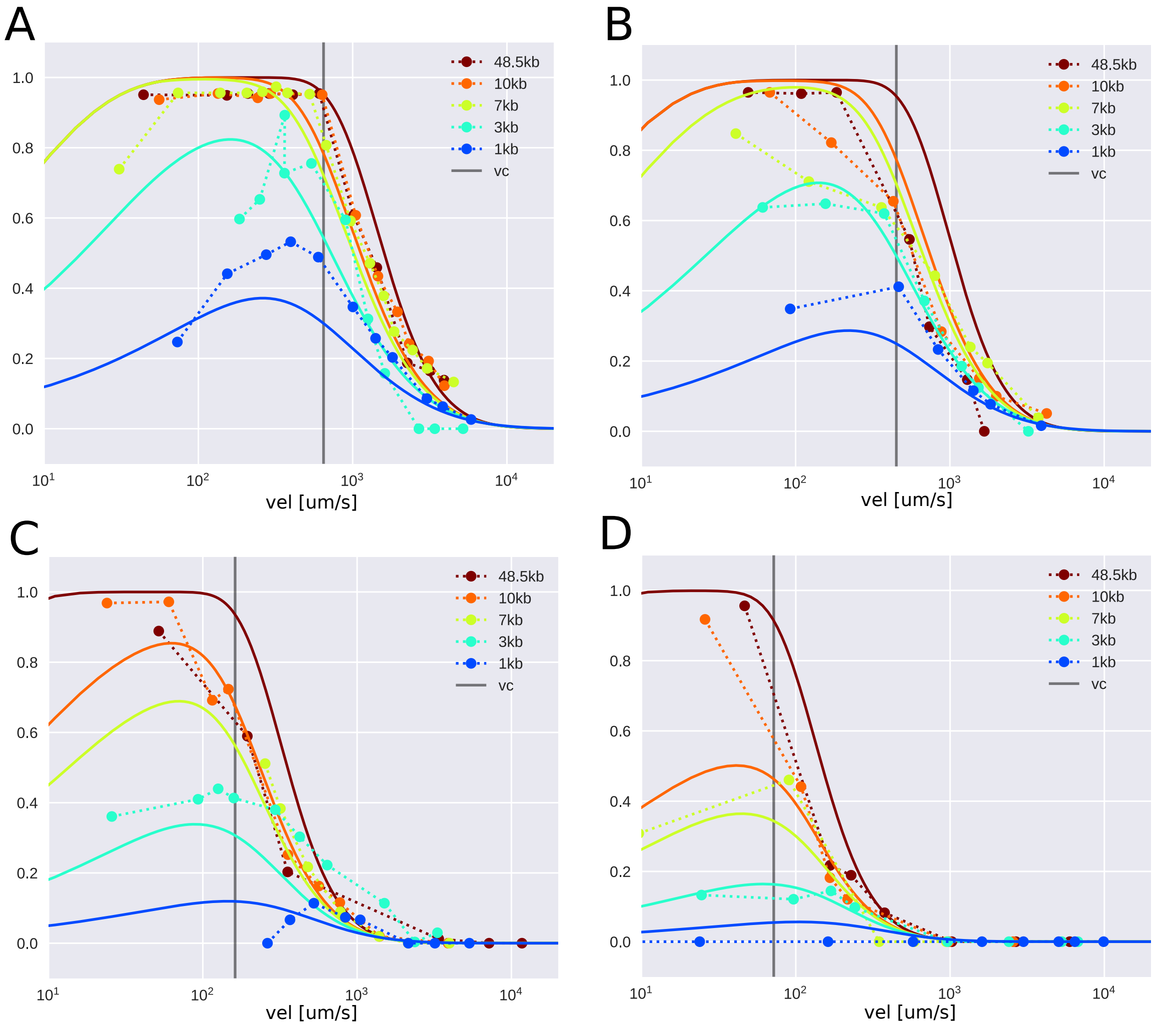

Figure 13: Numerical calculation of displacement efficiency, η, as a function of flow velocity for selected dsDNA fragment lengths, and for all gap sizes G tested (solid line). Experimental values are shown for comparison (closed circles, dash lines). v_c is the transition velocity calculated by Weissenberg number.

11 Velocity Tuning of dsDNA

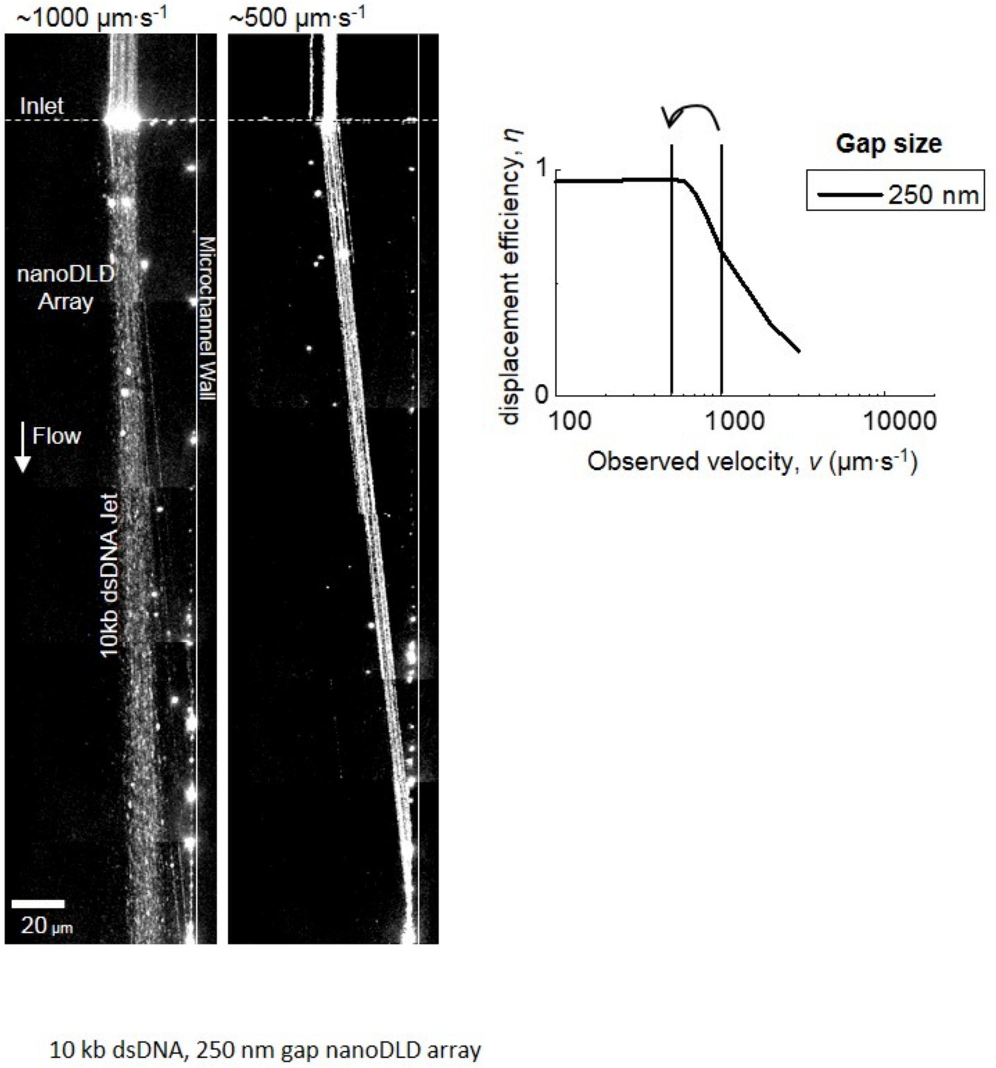

Figure 14: Fluorescence micrograph mosaics of 10 kb dsDNA in a G = 250 nm array at $v \sim 500$ and 1000 $\mu m\ s^{-1}$, demonstrating the ability to alter the migration angle θ through fluid velocity control. The inset flow shows the displacement efficiency curve, η, for 10 kb dsDNA, indicating the switch in displacement with the change in velocity.

12 Separation Resolution of dsDNA in nanoDLD

Separation in nanoDLD can occur when a mixture of particles is injected as a jet with a cross-section smaller than the width of the array. This leaves empty fluid volume into which displaced particle density can laterally translocated, effecting physical separation of the particles from those that follow the zigzag mode. To quantify this, separation resolution in the nanoDLD, R, was based on a chromatographic definition of resolution:

$$R = \frac{y_1 - y_2}{\frac{1}{2}(W_1 + W_2)} \tag{10}$$

This equation is based on the binary separation of two particle sizes, $D_{p1} > D_{p2}$. Assume the initial binary mixture is injected as a Gaussian with lateral peak width W_0 and mode y_0, and that both particles deflect at a migration angle in the DLD array with migration angles θ_1 and θ_2. When the particle jet flows axially a distance x, each component particle size will displace with a migration angle $\theta_1 > \theta_2$, separating the particle densities into two jets with cross-sections of peak width W_1 and W_2 and modes y_1 and y_2. The peak widths W must be approximated based on the particle distribution. For distributions approximated by Gaussians, $W \sim 0.42sw$, with s the number of standard deviations chosen to describe the peak width and w the full width at half maximum. A R = 1 is sufficient to ensure separation of s standard deviations between the peak modes. For the work here, s = 6, giving at R = 1 an overlap in the two DNA fragment distributions of 0.27%.

For experimental resolution analysis of dsDNA in the nanoDLD, particle samples were focused injected into the side of the device, opposite the collection wall, to allow the widest width and length of free fluid to separate into. Initial fluorescence profiles at the inlet generally could not be approximated as Gaussians, and required using the asymmetric double sigmoidal function F for fitting:

$$F = F_0 + A_f \left[1 + e^{\frac{y - y_c + \frac{w_1}{2}}{w_2}}\right]^{-1} \left(1 - \left[1 + e^{-\frac{y - y_c + \frac{w_1}{2}}{w_3}}\right]^{-1}\right) \tag{11}$$

With A_f the amplitude, y the lateral position, y_c the mode of the peak, and w_i the three fitting widths. For these approximation fits, the peak width was taken as the largest of the three w_i. After the DNA jet(s) has traversed $x = 0.1L$ length, it would generally form a cross-section that could be approximated as a Gaussian.

When DNA fragments have different θ it is feasible to increase R by using a longer length nanoDLD array. For a binary mixture of two DNA fragments injected as a jet with a Gaussian cross-section, at a flow velocity v, and migration angles $\theta_1 > \theta_2$ the lateral distance between the two distribution tails, d, at a given axial position x along the lenght of the array is given by:

$$\begin{aligned} d &= y_L 1 - Y_R 2 \\ &= -W_0 + x(tan\theta_1 - tan\theta_2) - \frac{n}{2^{\frac{1}{2}} v^{\frac{1}{2}}} x^{\frac{1}{2}} \left(D_y 1^{\frac{1}{2}} + D_y 2^{\frac{1}{2}}\right) \\ &= -W_0 + \beta + \gamma \end{aligned} \tag{12}$$

Where y_{L1} and y_{R2} are the end positions of the trailing and leading peak tails, respectively. β describes the difference in lateral displacement between the two DNA fragments and γ is the modification in the peak widths due to the diffusion of the DNA within the array. The two lateral diffusivities, $D_y 1$ and $D_y 2$, are not in general given by the Stokes-Einstein Relation. Cebeli *et al* [2, 1] have shown that lateral diffusion in DLD arrays can be an order of magnitude larger than bulk diffusion, due to the direction mode locking effect amplifying small deviations in position due to diffusion. Solving for the condition $d = 0$ at $R = 1$:

$$L_1 = \left[\frac{\gamma}{2\beta} \pm \left((\frac{\gamma}{2\beta})^2 + \frac{W_0}{\beta} \right) \right]^2 \tag{13}$$

With L_1 being the array length necessary for R = 1 separation. The factor $L_d = (\frac{\gamma}{2\beta})^2$ defines the axial distance at which lateral displacement begins to separate the two peak modes, overcoming the widening of the peak widths due to diffusion. Theoretically, a nanoDLD array can always be lengthened to allow separation of two species, regardless of the lateral diffusivities. Practically, in the case of pressure driven flow as in the current work, increasing the array length becomes restrictive due to hydrodynamic resistance, but may be less of a constraint for electrophoretically driven systems.

From the resolution data it is possible to measurement the lateral diffusivity of the dsDNA. Measurement of the peak width of the lateral profile as a function of axial position, x, along the array provides an estimate of the diffusion. Using a Gaussian approximation to the cross-sectional profile, $W = 6\sigma$, with σ the standard deviation of the distribution. Taking $\sigma = \sqrt{\frac{2xD_y}{v}}$, a plot of variance σ^2 versus x/v yields the lateral diffusivity as the linear slope. Tables 4 and 5 show the measured lateral diffusivities for selected dsDNA fragment lengths, showing a maximum observed $D_y \sim 50\ \mu\ m^2 s^{-1}$. The values obtained are 10-100x larger than the estimated bulk diffusivity for the dsDNA. Using these diffusivites to estimate the lower bound for separation, given L = 500 μm, at the maximum observed D_y, this implies $\theta_1 - \theta_2 \sim 0.5$. This proves a practical limit of dsDNA separation for DNA fragments of 100 bp and 200 bp for the current implementation down to the tested G = 219-250nm, based on the measured displacement efficiencies and the requirement to stay below $v \sim 1000\ \mu ms^{-1}$ due to the coil-stretch transition.

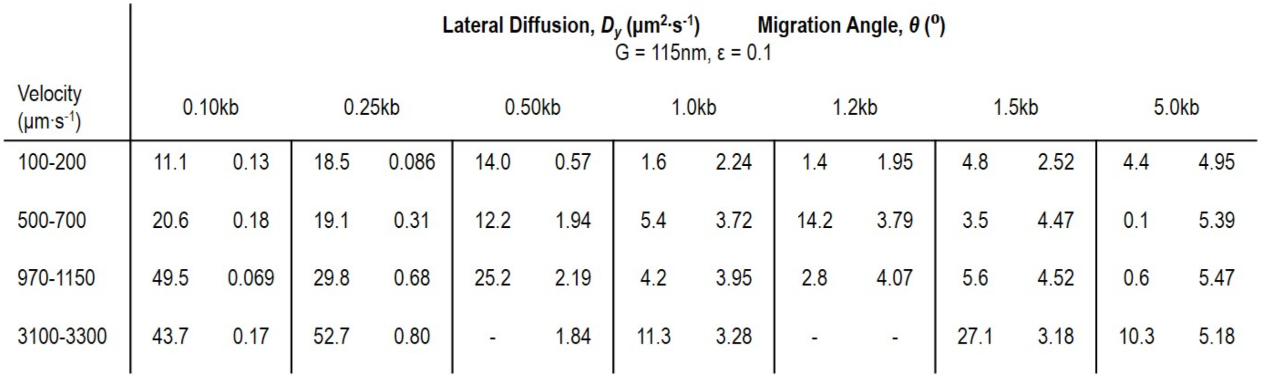

Velocity (μm·s^{-1})	Lateral Diffusion, D_y (μm^2·s^{-1}) Migration Angle, θ (^{o}) G = 115nm, ε = 0.1													
	0.10kb		0.25kb		0.50kb		1.0kb		1.2kb		1.5kb		5.0kb	
100-200	11.1	0.13	18.5	0.086	14.0	0.57	1.6	2.24	1.4	1.95	4.8	2.52	4.4	4.95
500-700	20.6	0.18	19.1	0.31	12.2	1.94	5.4	3.72	14.2	3.79	3.5	4.47	0.1	5.39
970-1150	49.5	0.069	29.8	0.68	25.2	2.19	4.2	3.95	2.8	4.07	5.6	4.52	0.6	5.47
3100-3300	43.7	0.17	52.7	0.80	-	1.84	11.3	3.28	-	-	27.1	3.18	10.3	5.18

Table 4: Lateral diffusivity, D_y and migration angle θ measured in a G = 115nm nanoDLD array, for selected dsDNA fragments, as a function of velocity. Velocities were chosen to sample behavior in the diffusion dominated regime (100-200 $\mu m\ s^{-1}$), before the migration angle drop-off, < v_c (500-700 $\mu m\ s^{-1}$), after the migration angle drop-off (coil-stretch transition onset), > v_c (970-1150 $\mu m\ s^{-1}$), and high velocity (3100-3500 $\mu m\ s^{-1}$). Absent values were not measured.

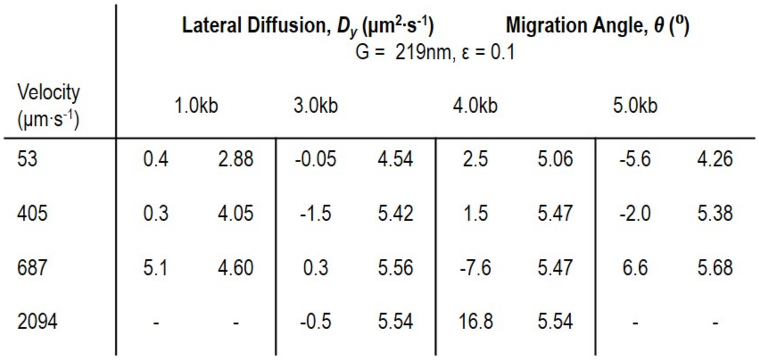

Velocity (μm·s^{-1})	Lateral Diffusion, D_y (μm^2·s^{-1}) Migration Angle, θ (^{o}) G = 219nm, ε = 0.1							
	1.0kb		3.0kb		4.0kb		5.0kb	
53	0.4	2.88	-0.05	4.54	2.5	5.06	-5.6	4.26
405	0.3	4.05	-1.5	5.42	1.5	5.47	-2.0	5.38
687	5.1	4.60	0.3	5.56	-7.6	5.47	6.6	5.68
2094	-	-	-0.5	5.54	16.8	5.54	-	-

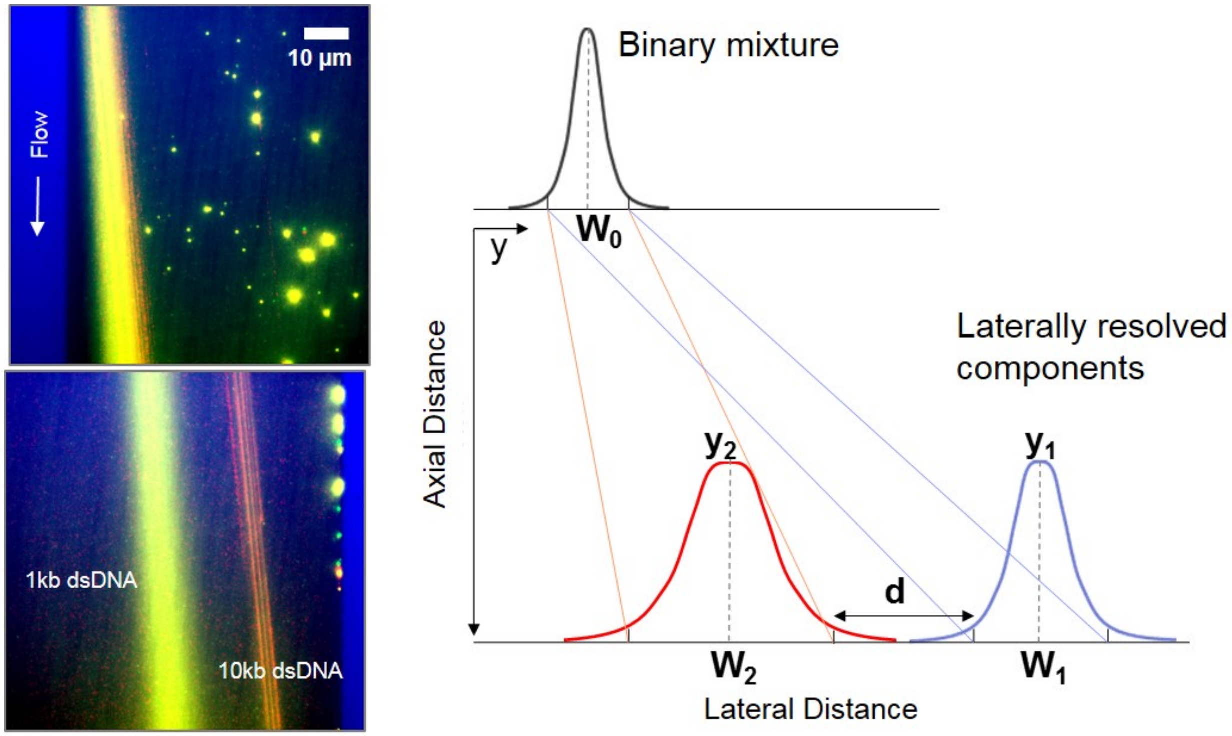

Figure 15: Separation resolution in nanoDLD. **(a)** Fluorescence micrographs of a binary mixture of 1 kb and 10 kb dsDNA fragments injected as a single stream into a $G = 219$ nm array, showing the separation of the initial jet into two separate jets, each of dsDNA of a given basepair size, demonstrating the separation capability of nanoDLD for dsDNA. **(b)** Schematic of phenomenological model for defining the separation resolution. For a binary mixture, the initial lateral cross-section of DNA density is approximated as a peak with mode y_0 and peak width W_0. After traversing x axial length down the array, the lateral displacement of the two DNA fragment populations leads to a splitting of the jet, and two cross-sections with modes y_1 and y_2 and peak widths W_1 and W_2. Separation occurs when the two peaks deconvolute laterally, generating DNA jets of a single species. The separation between the two peaks can be described by the variable d, which is the distances between the nearest tails of each particle distribution.

Table 5: Lateral diffusivity, D_y and migration angle θ measured in a $G = 115$nm nanoDLD array, for selected dsDNA fragments, as a function of velocity. Velocities were chosen to sample behavior in the diffusion dominated regime (100-200 $\mu m\ s^{-1}$), before the migration angle drop-off, $< v_c$ (500-700 $\mu m\ s^{-1}$), after the migration angle drop-off (coil-stretch transition onset), $> v_c$ (970-1150 $\mu m\ s^{-1}$), and high velocity (3100-3500 $\mu m\ s^{-1}$). Absent values were not measured.

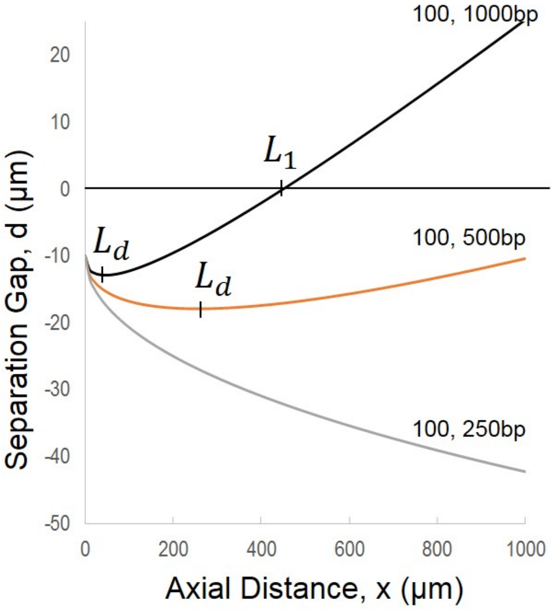

Figure 16: Plot of the lateral separation distance between particle distributions, d, as a function of axial position along the array x, showing the parameters L_d at which resolution begins to occur, and L_1, at which the separation resolution $R = 1$. d is plotted for different combinations of dsDNA fragments in a $G = 219$nm array, using experimentally measured migration angles and lateral diffusivities, showing that the 100 bp, 250 bp binary mixture is approximately the limit of separation in these arrays at length $L = 1000\mu m$.

13 Extraction and Quantification of dsDNA from nanoDLD using qPCR

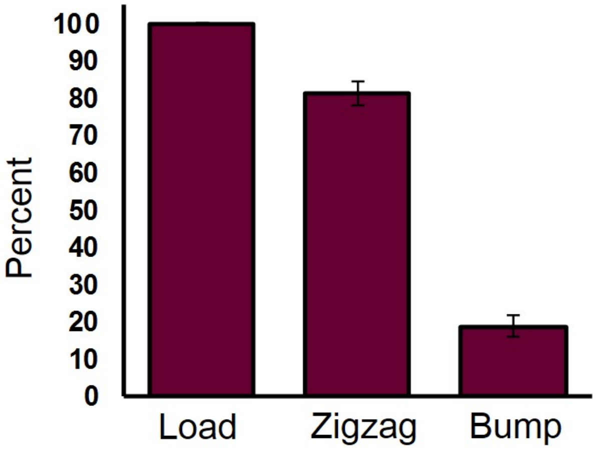

Figure 17: Percentage volume of processed dsDNA fragment solution collected from nanoDLD device. the zigzag and bump fractions (from outlets) have been normalized by the total volume injected at input (load).

14 Flow velocity of nanoDLD Arrays

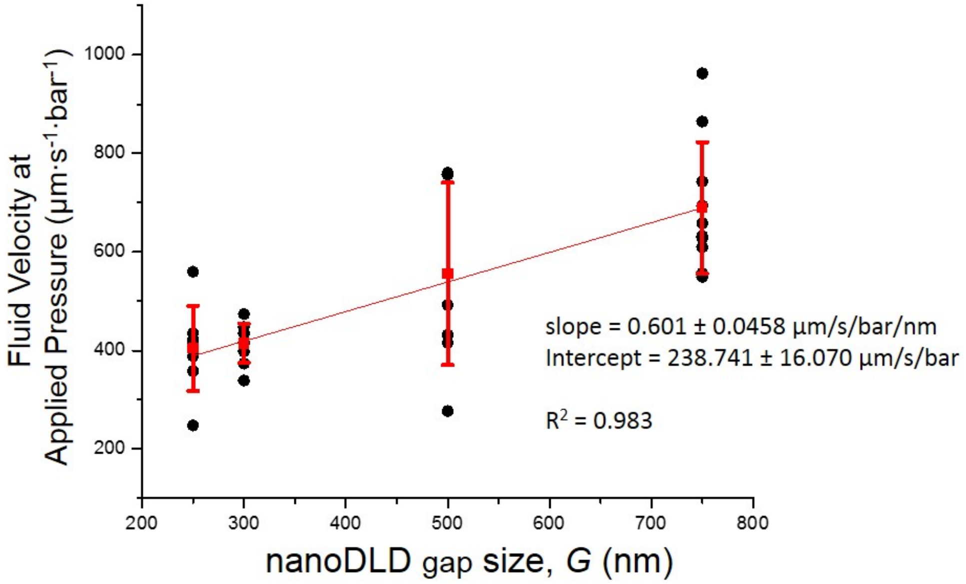

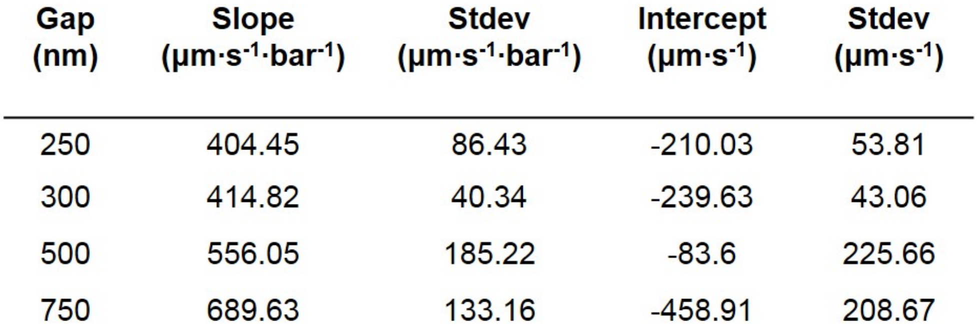

Gap (nm)	Slope ($\mu m \cdot s^{-1} \cdot bar^{-1}$)	Stdev ($\mu m \cdot s^{-1} \cdot bar^{-1}$)	Intercept ($\mu m \cdot s^{-1}$)	Stdev ($\mu m \cdot s^{-1}$)
250	404.45	86.43	-210.03	53.81
300	414.82	40.34	-239.63	43.06
500	556.05	185.22	-83.6	225.66
750	689.63	133.16	-458.91	208.67

Figure 18: Flow velocity of nanoDLD arrays. The flow velocity per applied pressure is plotted for each gap size tested for the velocity dependent data. The velocity was estimated from single particle tracking of individual dsDNA particles at low pressure values. The flow velocity as a function of applied pressure was calculated from a linear fit, under the assumption it remains a constant within the pressure range used, 0-15 bar.

15 Supporting Information Videos

1. **100bp - G250 - inlet.avi**: 100bp YOYO-1 dyed dsDNA full-width injection into a G = 250nm nanoDLD array. 100x magnification, 470ex/510em, 133frames, 40fps, exposure time 18ms, 1ng μL^{-1}.

2. **100bp - G250 - outlet.avi**: 100bp YOYO-1 dyed dsDNA flux from outlet of G = 250nm nanoDLD full-width injection array. 100x magnification, 470ex/510em, 129frames, 40fps, exposure time 18ms, 1ng μL^{-1}.

3. **1kb - G250 - inlet.avi**: 1,000bp YOYO-1 dyed dsDNA full-width injection into a G = 250nm nanoDLD array. 100x magnification, 470ex/510em, 88frames, 40fps, exposure time 18ms, 1ng μL^{-1}.

4. **1kb - G250 - outlet.avi**: 1,000bp YOYO-1 dyed dsDNA flux from outlet of G = 250nm nanoDLD full-width injection array. 100x magnification, 470ex/510em, 98frames, 40fps, exposure time 18ms, 1ng μL^{-1}.

5. **10kb - G250 - inlet.avi**: 10,000bp YOYO-1 dyed dsDNA full-width injection into a G = 250nm nanoDLD array. 100x magnification, 470ex/510em, 79frames, 40fps, exposure time 18ms, 1ng μL^{-1}.

6. **10kb - G250 - outlet.avi**: 10,000bp YOYO-1 dyed dsDNA flux from outlet of G = 250nm nanoDLD full-width injection array. 100x magnification, 470ex/510em, 97frames, 40fps, exposure time 18ms, 1ng μL^{-1}.

7. **500bp - G250 - slowdown.avi**: Video of 500bp YOYO-1 dyed dsDNA flux as the flow velocity, v, is slowed from $\sim 5000\mu m$ s^{-1} to $< 100\mu m$ s^{-1} in a G = 250nm full-width injection array, demonstrating the velocity dependence on migration angle θ. DNA only achieves a partial bump mode while slowing down, before entering full zigzag mode, demonstrating the phenomenon of a local maximum in displacement at v_m for this fragment size. 100x magnification, 470ex/510em, 125frames, 10fps, exposure time 18ms, 1ng μL^{-1}.

8. **1kb - G250 - slowdown.avi**: Video of 1,000bp YOYO-1 dyed dsDNA flux as the flow velocity, v, is slowed from $\sim 5000\mu m$ s^{-1} to $< 100\mu m$ s^{-1} in a G = 250nm full-width injection array, demonstrating the velocity dependence on migration angle θ. Comparison of maximum achieved migration angle (displacement) of 1,000bp to 500bp (SI Appendix, video 7) shows the change in maximum displacement with fragment length. 100x magnification, 470ex/510em, 143frames, 10fps, exposure time 18ms, 1ng μL^{-1}.

9. **lambda - G250 - v287.avi**: Periodic pattern & capture - Lambda phage genome, 48.1kb YOYO-1 dyed, flowing into a G = 250nm full-width injection nanoDLD array at $v = 287\mu m$ s^{-1}. 100x magnification, 470ex/510em, 80frames, 40fps, exposure time 18ms, 100pg μL^{-1}.

10. **lambda - G250 - v2260.avi**: Periodic pattern & capture - Lambda phage genome, 48.1kb YOYO-1 dyed, flowing into a G = 250nm full-width injection nanoDLD array at $v = 2260\mu m$ s^{-1}, demonstrating the periodic intensity pattern in individual particle trajectories, as well as the capture and temporary immobilization of DNA fragments at higher speeds. 100x magnification, 470ex/510em, 82frames, 40fps, exposure time 18ms, 100pg μL^{-1}.

11. **10kb - G219 - forward inlet.avi**: Reverse flow experiment - 10,000bp YOYO-1 dyed dsDNA focused injected at the inlet into a G = 250nm nanoDLD array at the micro-channel wall opposite the collection wall. 100x magnification, 470ex/510em, 174frames, 40fps, exposure time 18ms, 10ng μL^{-1}.

12. **10kb - G219 - forward outlet.avi**: Reverse flow experiment - 10,000bp YOYO-1 dyed dsDNA focused injected into a G = 250nm nanoDLD array at the outlet, near the collection wall, showing full bumping. 100x magnification, 470ex/510em, 173frames, 40fps, exposure time 18ms, 10ng μL^{-1}.

13. **10kb - G219 - reverse inlet.avi**: Reverse flow experiment - 10,000bp YOYO-1 dyed dsDNA which has passed through a G = 250nm nanoDLD array and is now being flowed in reverse, through the outlet interface, back through the same array. 100x magnification, 470ex/510em, 134frames, 40fps, exposure time 18ms, 10ng μL^{-1}.

14. **10kb - G219 - reverse outlet.avi**: Reverse flow experiment - 10,000bp YOYO-1 dyed dsDNA exiting at the inlet of a G = 250nm nanoDLD array after being passed twice through the array, demonstrating full bumping with no major partial bumping events, giving evidence of the nanoDLD does not fragment DNA substantially during processing. 100x magnification, 470ex/510em, 200frames, 40fps, exposure time 18ms, 10ng μL^{-1}.

15. **resolution - G219 - inlet.avi**: Separation resolution demonstration - Mixture of 100bp, 1,000bp, and 10,000bp YOYO-1 dyed dsDNA (1:4:4 v:v:v ratio, 10ng μL^{-1}) focus injected at the inlet into a G = 250nm nanoDLD array at the micro-channel wall opposite the collection wall. 100x magnification, 470ex/510em, 105frames, 40fps, exposure time 18ms.

16. **resolution - G219 - array.avi**: Separation resolution demonstration - Mixture of 100bp, 1,000bp, and 10,000bp YOYO-1 dyed dsDNA (1:4:4 v:v:v ratio, 10ng μL^{-1}) focus injected into a G = 250nm nanoDLD array, showing the separation of the mixed DNA particle stream into separate fluxes based on migration angle θ. The video is captured $\sim$ half-way through the array. 100x magnification, 470ex/510em, 94frames, 40fps, exposure time 18ms.

17. **resolution - G219 - outlet1.avi**: Separation resolution demonstration - Mixture of 100bp, 1,000bp, and 10,000bp YOYO-1 dyed dsDNA (1:4:4 v:v:v ratio, 10ng μL^{-1}) focus injected into a G = 250nm nanoDLD array, showing the flux at the outlet of the 100bp (left) and 1,000bp (right) DNA fragments. 100x magnification, 470ex/510em, 166frames, 40fps, exposure time 18ms.

18. **resolution - G219 - outlet12.avi**: Separation resolution demonstration - Mixture of 100bp, 1,000bp, and 10,000bp YOYO-1 dyed dsDNA (1:4:4 v:v:v ratio, 10ng μL^{-1}) focus injected into a G = 250nm nanoDLD array, showing the flux at the outlet of the 100bp (left) and 1,000bp (center) and 10,000bp (right) DNA fragments. 100x magnification, 470ex/510em, 157frames, 40fps, exposure time 18ms.

19. **extraction - 2kb - injection.avi**: Extraction experiment - Inlet region of extraction nanofluidic chip, showing the flux of lambda phage genome HindIII digest 2.0kb dsDNA fragment, YOYO-1 dyed 10ng μL^{-1}, into the nanoDLD arrays. 10x magnification, 470ex/510em, 82frames, 40fps, exposure time 0.1s.

20. **extraction - 2kb - bump fraction.avi**: Extraction experiment - Outlet region of extraction nanofluidic chip, showing the flux of fully bumped lambda phage genome HindIII digest 2.0kb dsDNA fragment,

YOYO-1 dyed 10ng μL^{-1}, moving toward output via for collection. 10x magnification, 470ex/510em, 83frames, 40fps, exposure time 0.1s.

References

[1] S. Cerbelli. “Critical dispersion of advecting-diffusing tracers in periodic landscapes of hard-wall symmetric potentials.” English. In: *Phys Rev E Stat Nonlin Soft Matter Phys* 87.6 (June 2013), p. 060102. DOI: `10.1103/PhysRevE.87.060102`.

[2] S. Cerbelli. “Separation of polydisperse particle mixtures by deterministic lateral displacement. The impact of particle diffusivity on separation efficiency”. English. In: *Asia-Pacific Journal of Chemical Engineering* 7.24 (2012), S356–S371. DOI: `10.1002/apj.1656`.

[3] Y. Chen et al. “Concentrating genomic length DNA in a microfabricated array.” English. In: *Phys. Rev. Lett.* 114.19 (May 2015), p. 198303. DOI: `10.1103/PhysRevLett.114.198303`.

[4] E. R. Dufresne, D Altman, and D. G. Grier. “Brownian dynamics of a sphere between parallel walls”. In: *Europhysics Letters (EPL)* 53.2 (2001), pp. 264–270. DOI: `10.1209/epl/i2001-00147-6`.

[5] P. G. de Gennes. “Coil-stretch transition of dilute flexible polymers under ultrahigh velocity gradients”. English. In: *J. Chem. Phys.* 60.12 (1974), pp. 5030–5042. DOI: `10.1063/1.1681018`.

[6] D. W. Inglis, M. Lord, and R. E. Nordon. “Scaling deterministic lateral displacement arrays for high throughput and dilution-free enrichment of leukocytes”. In: *J. Micromech. Microeng.* 21.5 (2011), p. 054024. DOI: `10.1088/0960-1317/21/5/054024`.

[7] D. W. Inglis et al. “Critical particle size for fractionation by deterministic lateral displacement.” English. In: *Lab Chip* 6.5 (May 2006), pp. 655–658. DOI: `10.1039/b515371a`.

[8] E. Jones et al. *SciPy: Open source scientific tools for Python*. Tech. rep.

[9] S. C. Kim et al. “Broken flow symmetry explains the dynamics of small particles in deterministic lateral displacement arrays.” English. In: *Proc. Natl. Acad. Sci. U.S.A.* 114.26 (June 2017), E5034–E5041. DOI: `10.1073/pnas.1706645114`.

[10] B. Kundukad, J. Yan, and P. S. Doyle. “Effect of YOYO-1 on the mechanical properties of DNA”. English. In: *Soft Matter* 10.48 (2014), pp. 9721–9728. DOI: `10.1039/c4sm02025a`.

[11] J. F. Marko and E. D. Siggia. “Stretching DNA”. English. In: *Macromolecules* 28.26 (1995), pp. 8759–8770. DOI: `10.1021/ma00130a008`.

[12] W. W. Reisner, J. N. Pedersen, and R. H. Austin. “DNA confinement in nanochannels: physics and biological applications.” English. In: *Rep Prog Phys* 75.10 (Oct. 2012), p. 106601. DOI: `10.1088/0034-4885/75/10/106601`.

[13] C. Wang et al. “Hydrodynamics of Diamond-Shaped Gradient Nanopillar Arrays for Effective DNA Translocation into Nanochannels”. English. In: *ACS Nano* 9.2 (2015), pp. 1206–1218. DOI: `10.1021/nn507350e`.

[14] B. H. Wunsch et al. “Nanoscale lateral displacement arrays for the separation of exosomes and colloids down to 20nm.” English. In: *Nat Nanotechnol* 11.11 (Nov. 2016), pp. 936–940. DOI: `10.1038/nnano.2016.134`.